Master's thesis and Internship : Integration of a supercritical carbon dioxide cycle with a solid oxide electrolyser

Auteur : Roomans, Noam
Promoteur(s) : Lemort, Vincent; 30030
Faculté : Faculté des Sciences appliquées
Diplôme : Master : ingénieur civil en génie de l'énergie à finalité spécialisée en Energy Conversion
Année académique : 2025-2026
URI/URL : http://hdl.handle.net/2268.2/26206

University of Liege
Faculty of Applied Sciences
Academic year 2025-2026

ALMA MATER STUDIORUM
UNIVERSITÀ DI BOLOGNA

Integration of a supercritical carbon dioxide cycle with a solid oxide electrolyser

Master thesis submitted in partial fulfillment of the requirements for the Master's degree in Energy Engineering

by **Roomans Noam**

Promoter:
LEMORT Vincent

Jury:
LEMORT Vincent
DE PASCALE Andrea
GENDEBIEN Samuel

Supervisors:
DE PASCALE Andrea
ROSATI Francesca

Acknowledgments

First of all, I would like to thank my promoter, Professor Lemort, for his help and support throughout my work, as well as for the opportunity he gave me by putting me in touch with my supervisor, Professor De Pascale.

Next, I would like to thank my supervisor, Professor De Pascale, for his guidance and explanations during this research internship at the University of Bologna. I am also grateful to Francesca Rosati for her support throughout my internship and for her help in reviewing every part of my work. Also, I would like to thank Elise Neven as well for her valuable feedback.

Finally, I would like to thank Griffin Scullino for his help as a proofreader, as well as my parents and friends for their support.

Abstract

Hydrogen production via solid oxide electrolysis (SOE) is the most efficient production method to produce green hydrogen, but its high temperature operation requires a significant energy demand. While SOE system-level optimisation studies only consider heat integration and recovery between high and low temperature streams within the process, the potential advantage of a bottoming power cycle on the high-temperature anode side exhaust remains uninvestigated.

This work first defines the base process by modifying a previous model in Aspen HYSYS™ and putting in alignment with designs in the literature. Afterwards, two steady-state models of a supercritical carbon dioxide Brayton cycle are modelled in EES. Finally, the anode side of the electrolyser is chosen as the location of integration for the sCO_2 cycle. This integration is then assessed under two different analyses: an exergy one and a primary energy one. From an exergetic perspective, using a power cycle increases the exergy destruction within the system compared to the base case without any bottoming cycle. The results from the primary energy analysis show that the primary energy consumption of the system can be decreased by 0.7% using a simple recuperative sCO_2 bottoming cycle and by 1.17% using a recompressed recuperative one. Finally, a scenario in which the cycle net power is maximised is considered, and it turns out that the cycle can cover up to 20% of the electrolyser's electricity consumption.

Contents

List of Figures

List of Tables

Chapter 1

Introduction

In the last decade, the growth of renewable energy sources (RES) for electricity production has significantly increased, as has their penetration in electricity grids. The share of RES in the European Union for electricity production was 48% [1] in 2024. By 2030, the EU's target for electricity production from renewables is 69% [2].
Due to their inherent intermittent nature, RES pose several problems for electrical network stability. Indeed, the electrical demand does often not match the production, leading to the use of curtailment to avoid a balance problem. In 2025, Germany, France, and the Netherlands curtailed 3.9 TWh of renewable energy [3]. This therefore represents a pure loss of energy. The International Energy Agency (IEA) highlighted the increase of renewable energy curtailment because of the increase of RES [4], as depicted in Fig. 1.1.

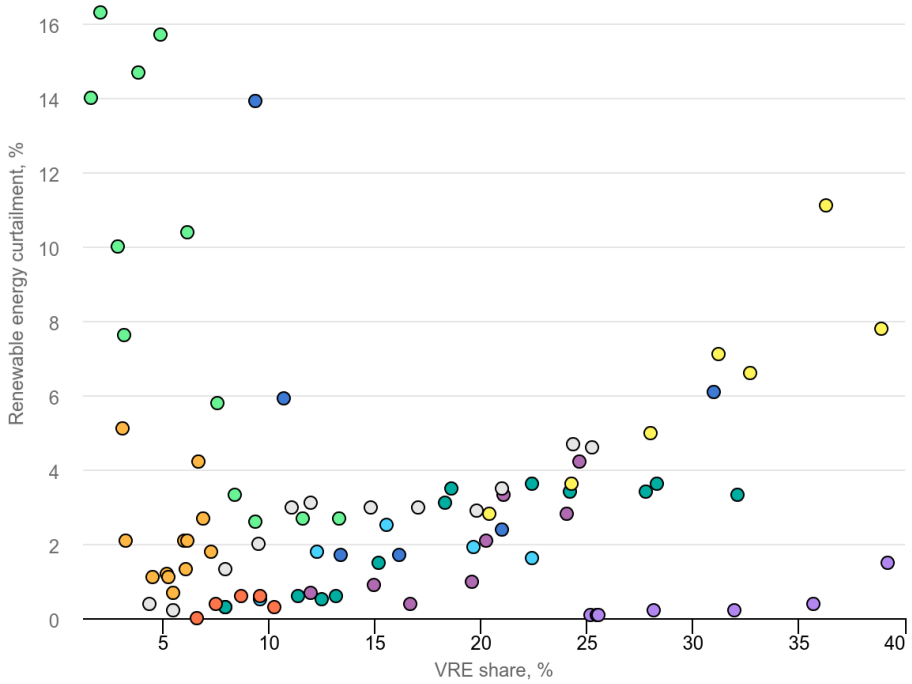

Figure 1.1: *Renewable energy curtailment as a function of variable renewable energy (VRE) for different countries, each represented by a colour, from [4].*

Considering the expected increase of the penetration of RES in coming years, batteries are a solution, capable of storing electricity when the production is in surplus and supplying the grid when production is in deficit.

Among different batteries technologies, power-to-gas (P2G) consists in converting electricity into chemical energy. It offers great advantages over other storage mechanisms, as P2G enables the storage of significant amounts of energy over long periods, making seasonal storage possible [5]. The technology can therefore be used to produce storable synthetic fuels such as hydrogen, methane, or synthetic natural gas (SNG). The advantages with SNG are threefold. SNG is easily transportable over large distances using pipelines. The natural gas pipeline infrastructure already exists, which removes the need to construct a new distribution system. If SNG is injected directly into the distribution network, this makes the storage capacity infinite [6]. Power-to-power (P2P) includes P2G as an initial phase, but it also includes a second part during which the converted synthetic gas is transformed back to electricity.

The project in which this work takes part is *LA 1.2 - Studio di cicli termodinamici complessi per l'integrazione termica con SOE al servizio di rinnovabili elettriche e fonti termiche*, which consists of optimising the thermal recovery within a reversible solid oxide cell (r-SOC) in charge mode, which corresponds to a solid oxide electrolyser cell (SOEC). The latter enables electricity storage in the form of hydrogen.

The current project and model of the r-SOC stems from the research *LA 2.27 – Modellazione finalizzata allo scale-up di un sistema Power-toGas-to-Power basato su r-SOC e reattore di metanazione bidirezionale*, from Ancona et al. [5]. Their research is conducted by researchers from the University of Bologna for the CNR-ITAE and focuses on developing a P2P system, the simplified diagram of which is shown in Fig. 1.2. The project is centred around two components: a reversible Solid Oxide Cell (r-SOC) and a reversible chemical reactor (RCR) working both as a reformer and methanator. The idea is to produce synthetic fuels when the electric grid is in surplus (charge phase) and convert that fuel back to electricity for periods of deficit (discharge phase). In charge phase, water is electrolysed by the r-SOC. The produced hydrogen is further used in the methanator (RCR unit) to be transformed into synthetic methane. During discharge phase, the reformer (RCR unit) converts the synthetic methane into hydrogen. Therefore, the r-SOC works as a fuel cell to produce electricity from this hydrogen. The full system is modelled in Aspen HYSYS™ and calibrated using experimental data measured on a SolydEra G8 r-SOC stack at the CNR-ITAE laboratory.

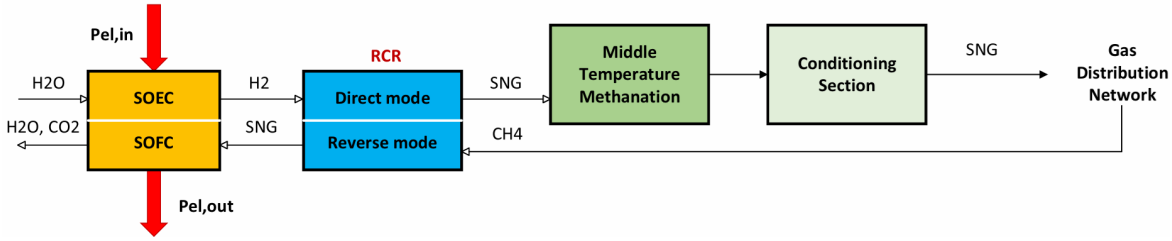

Figure 1.2: *Simplified schematic of the previous P2P system based on the two key reversible devices, from [5].*

The previous project has demonstrated some achievements. The authors showed that when the high temperature electrolysis and the methanation are thermally integrated, it results in significant energy savings. Using a heat recovery section, the system can use water from the RCR to preheat the inlet water for electrolysis. In electric-to-fuel (E2F), the efficiency of the process is about 82%, while in the fuel-to-electric (F2E), the efficiency is 46%. In total, the P2P round-trip efficiency is 38%.

The objective of this thesis is to assess the potential benefit from the integration of a bottoming cycle within the r-SOC when functioning as an electrolyser. In the current design, high temperature streams from the electrolyser at 700°C are directly used to preheat inlet streams for the process. Instead of thermally integrating these high temperature streams, the idea is to power a bottoming cycle and take

advantage of this high quality energy. The electricity produced by the cycle would then decrease the process net electricity consumption.

1.1 Electrolysis description

In this section, the theoretical foundations of electrolysis are detailed. The superior efficiency of SOEC compared to other technologies is first illustrated. Then, the theoretical operation of SOEC is clarified.

1.1.1 SOEC superior efficiency

Water electrolysis consists of providing electrical energy to split water into hydrogen and oxygen.

$$2H_2O \rightarrow 2H_2 + O_2 \tag{1.1}$$

Different electrolysis stack technologies exist, but three of them in particular stand out: alkaline electrolysis stacks (AEC), proton exchange membrane electrolysis stacks (PEMEC) and SOEC. While the overall chemical reaction is the same in all three stacks, the first two operate at a lower temperature range, respectively 60–80 °C and 50–80 °C, whereas SOEC technology works in the much higher range of 700–900 °C [7]. In practice, this leads to a significant reduction in electrical consumption for SOECs compared to the other two stack types for the same amount of hydrogen produced.

The energy demand for the electrolysis reaction can be expressed as

$$\Delta H = \Delta G + T\Delta S \tag{1.2}$$

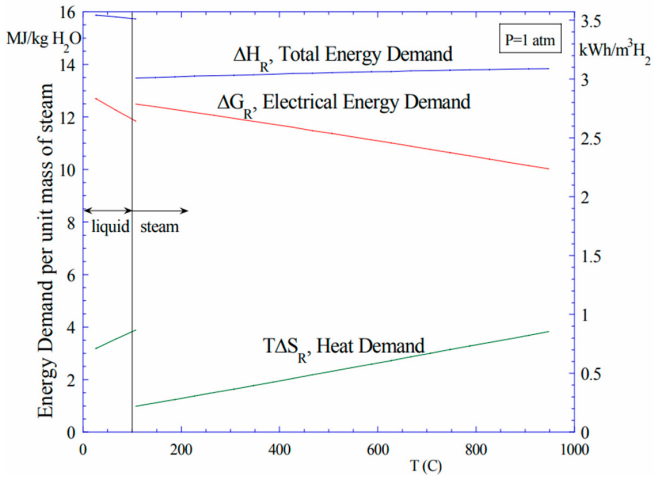

Figure 1.3: *Water electrolysis energy demand as a function of temperature, from [8].*

The water-splitting reaction total energy (ΔH) is the sum of the Gibbs free energy (ΔG), which corresponds to the electrical energy required by the reaction, and the thermal energy required by the reaction ($T\Delta S$). In Fig. 1.3, it can be seen that the total energy slightly increases on the considered temperature range whilst the electrical energy demand decreases considerably. The high temperature operation of SOECs takes advantage of this behaviour to minimise the electrical demand of the process, which is the main reason explaining their higher performance compared to lower temperature technologies.

1.1.2 SOEC operation

A SOEC stack has inputs both at the anode and cathode as shown in Fig. 1.4. The cathode is fed with water and a recirculated fraction of hydrogen from the cathode outlet, preventing the cathode electrode from being oxidised and potentially damaged as a result [9]. Then, the parameter setting the quantity of water used is the steam conversion rate. It is defined as the ratio of the water consumed at the cathode to the water provided to the stack. If this value were equal to 1, no water would be available at the active area of the stack, causing reactant starvation, and consequently, damage to the stack [9]. Finally, at the anode, sweep air is fed for two reasons. It sweeps the produced oxygen away and avoids thermal gradient [9].

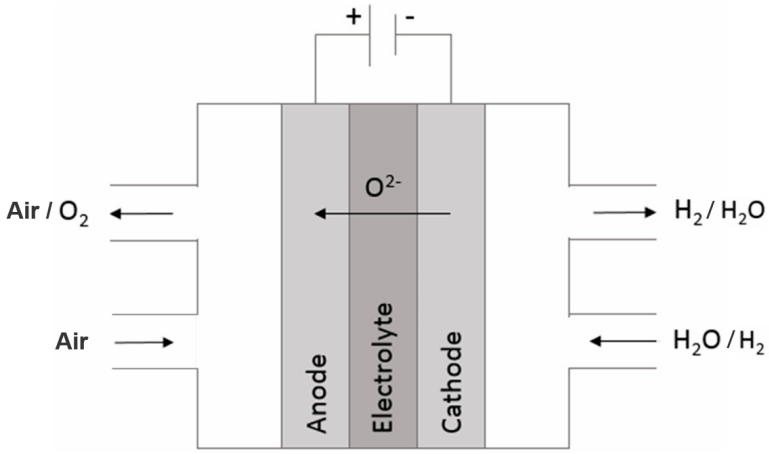

Figure 1.4: *SOEC simplified schematic, modified from [10].*

The thermal characteristics of the stack are a function of the operating voltage. The thermoneutral voltage represents the thermal equilibrium at which the heat required by the endothermic reaction is balanced by the heat generated by internal losses in the stack. The temperature of outlet and inlet streams is therefore equal. Outside thermoneutrality, the stack is either in endothermic or exothermic state, thus requiring external heating or cooling [7]. Considering the very high temperature of the outlet streams and the heating required for the feed streams, heat recuperation is essential. This can be achieved either by designing a heat exchanger network (as already implemented in this project) or, potentially, by integrating a bottoming power cycle to take advantage of the high-grade heat from the exhaust.

1.2 Process description

This section presents the already modelled electrolysis process by analysing its operating conditions and thermal characteristics.

The model depicted in Fig. 1.5 is a result from the work of Ancona et al [5]. The model developed in Aspen HYSYS™ assumes steady-state operation for the electrolyser unit working at 4.3 kW_e and at a temperature of 700°C. The high temperature streams of interest for the bottoming cycle are thus the cathode and anode output, both at 700°C and highlighted by a thick trait.

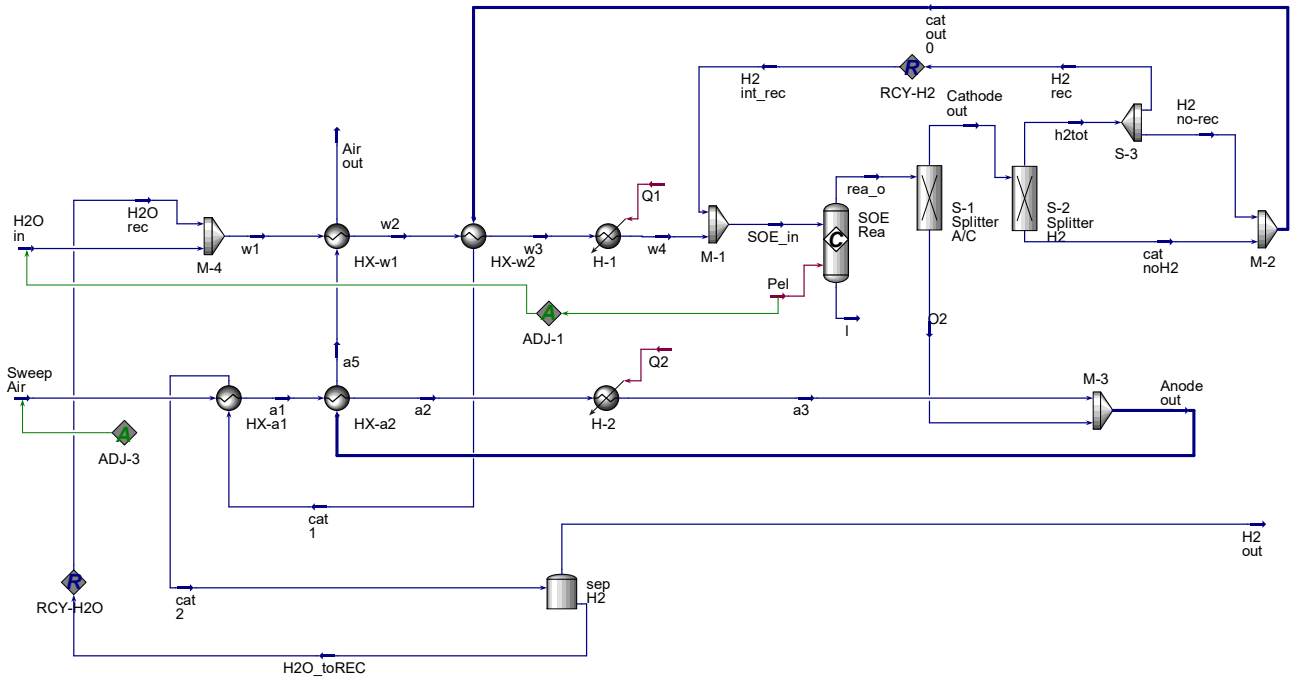

Figure 1.5: *Process flowsheet modelled in Aspen HYSYS™.*

As made clear in Fig. 1.5, the process has two feed streams: water (*H2O in*) and air (*Sweep Air*). The objective is to feed the stack with steam and use the sweep air for sweeping produced oxygen and avoiding oxidation of the anode as previously noted.

Inside the electrolyser, the steam conversion is set to 86%. A splitter S-1 models the products from electrolysis at the cathode and anode, respectively the mix of hydrogen and water, and the pure oxygen. The mixer M-3 output, *Anode out*, represents the sum of the pure oxygen and the sweep air. The splitter S-2 simulates the separation of hydrogen and water. The splitter S-3 is then used to recirculate a fraction of the hydrogen to prevent cathode deactivation. This recirculation is set to 11%. The recirculated hydrogen is sent to M-1 to be mixed with the feed steam. The remaining hydrogen, seen as the net produced hydrogen, is further mixed with the water in M-2. The stream *cat out 0* is therefore the net cathode output. Table 1.1 sets out the parameters specified in the process.

Table 1.1: *Process conditions in Aspen HYSYS™.*

Parameter	Value
Inlet H_2O temperature (°C)	25
Inlet H_2O pressure (kPa)	101.3
Stack temperature (°C)	700
Stack pressure (kPa)	100
Input power (kW)	4.3
Inlet H_2O flow rate (kg/h)	1.176
Conversion efficiency (%)	86
Inlet Sweep Air temperature (°C)	25
Inlet Sweep Air pressure (kPa)	100
O_2 molar fraction at anodic outlet (%)	25
H_2 recirculation rate (%)	11

The process has two outlet streams: *Air out* and *H2 out*. The first is a mix of pure oxygen and air while the second is the net produced hydrogen by the process.

On the sweep air line, *a2* corresponds to the sweep air stream after heat recuperation within HX-a2 while *a5* is the anode output stream after cooling in HX-a2. On the feed water line, *w1* is the mix of the recirculated water from the cathode and the input water in the process. The stream *w2* represents the feed water after a first preheating within HX-w1.
Evident in the flowsheet are four heat exchangers and two heaters. Considering the high operation temperature of the stack, heat recovery is important to preheat inlet streams. In their design, Ancona et al. [5] do not specify an effectiveness or a pinch point temperature difference (PPTD), but impose temperature to fully determine the heat exchangers. These temperatures are summarised in Table 1.2.

Table 1.2: *Streams with imposed temperature connected to the recuperation heat exchangers.*

Stream	Temperature (°C)
Air out	80
a2	540
cat 1	110

The heat exchangers are considered to be counter current and shell-and-tube. The exchanger HX-w2 preheats the feed water with the high temperature stream at the cathode outlet. HX-w1 preheats the feed water as well but uses the anode outlet stream as the hot source. Two temperatures are fixed for these two heat exchangers, the outlet air temperature at HX-w1 (*Air out*) and the outlet hydrogen/water mixture temperature of HX-w2 (*cat 1*). It is important to note that the feed water heating undergoes different kinds of heating in HX-w1 and HX-w2.
In Fig. 1.6a, it can be seen that sub-cooled water is heated and then evaporates. Due to this phase change stage, an internal pinch of 3 degrees appears. After this heat exchanger, it is shown in Fig. 1.6b that the water continues being evaporated and eventually gets superheated to a temperature of 542°C. The profile particularly shows a better match of the temperature profiles compared to HX-w1 as the latter evaporates water in large part. After HX-w2, the water is finally heated to the desired 700°C by the heater H-1. The heat source nature in H-1 and H-2 are unspecified.

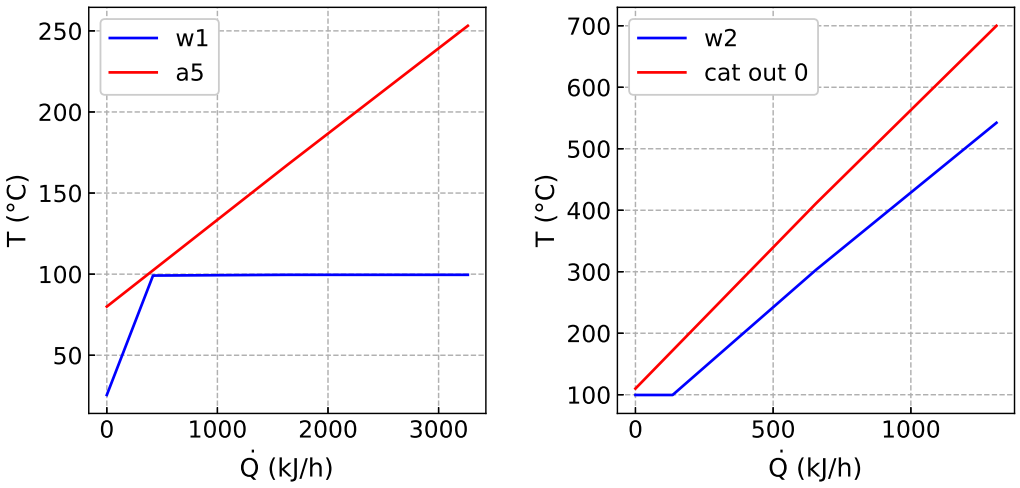

(a) *HX-w1.* **(b)** *HX-w2.*

Figure 1.6: *T-Q profiles in the heat exchangers on the feed water line.*

Then, the heat exchangers on the sweep air line can be analysed. The T-Q profiles are illustrated in Fig. 1.7.

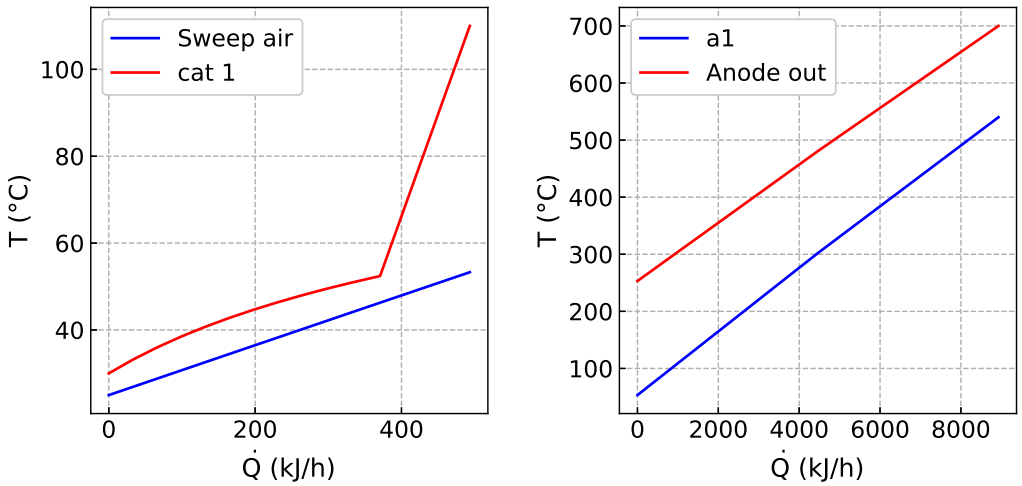

(a) *HX-a1.* **(b)** *HX-a2.*

Figure 1.7: *T-Q profiles in the heat exchangers on the sweep air line.*

The first noticeable difference between the two HXs is the amount of heat exchanged. Indeed, the thermal power exchanged is almost 20 times higher in HX-a2 than in HX-a1. In HX-a1, *cat* 1 consists of a mixture of steam and hydrogen. As the stream is being cooled, the water in the mixture starts to condense, which explains the sudden change of the hot stream slope. Regarding HX-a2, there is an approximately constant temperature difference between the two streams of 200°C. This high difference proves that this heat exchanger is not optimised. After HX-a2, the sweep air is heated up to 700°C by the external heater H-2.

From a global perspective, the process contains two streams wherein high temperature recuperation is done: the anode and cathode outlets. However, Table 1.3 shows that the heat capacity flow rate is much higher on the anode side. This demonstrates the higher importance of an efficient heat recuperation on this side.

Table 1.3: *Anode and cathode thermal characteristics.*

Stream	Temperature (°C)	Mass flow rate (kg/h)	Heat capacity rate (kJ/h·K)
cat out 0	700	0.307	2.31
Anode out	700	18.18	20.71

Chapter 2

Process modification

2.1 Literature review

This section presents the highest scale up existing integrations of solid oxide electrolyser (SOE) in order to assess the current development of high temperature electrolysis. After that, a review of more advanced integrations of SOE, such as with a bottoming power cycle for high temperature electrolysis, is presented.

In this work, the heat exchanger network of the current modelled process is expected to be simplified. To this end, a review of SOEC thermal integration is done.

Min et al. [7] provides a framework for the thermal integration of SOE systems. It defines the electrolysis process in three zones: a thermal energy receiving zone (inlet streams), a thermal energy supplying zone (hot exhaust streams) and external heat sources. The authors highlight the importance of thermal integration as maintaining high temperature is the original benefit of the high efficiency of an SOEC. According to the authors, the "rule of thumb" for an efficient design consists of using the high temperature outlet streams to preheat directly the inlet streams with the highest possible temperature.

As the inlet streams cannot be fully heated to the stack temperature by solely recuperating heat from exhaust gases, the design must integrate an external heat source. This external heat source can be classified in two categories: high-temperature (HT) and low-temperature (LT) [7]. The first category provides a complete heating of the inlet streams while the latter will be limited by its temperature [7]. In practice, HT waste heat sources are limited. As reported by the authors, industrial waste heat (metal and steel manufacturing) and municipal waste burning are the two current possible HT waste heat sources. LT sources, on the other hand, are more abundant [7].

The second largest scale SOEC industrial demonstration by power is from the GrInHy2.0 project [11]. This project integrated a solid oxide electrolyser, of 720 kW nominal power developed by Sunfire, in a steel plant. The waste heat generates steam for the electrolyser module for a total of 17.9% of the module consumption (thermal and electrical together). The LT requirements are thus provided with the waste heat while the HT by electrical heaters. The stack operates at 865°C.

The largest SOE installation to date is from the MultiPLHY project [12]. It consists of the integration of a 2.4 MW SOE, by Sunfire, within a biofuel refinery. Contrary to the previous case, where waste heat from the plant is used to generate steam for the SOE, the steam here is supplied from the refinery's existing utility steam network. With a hydrogen production rate of 60 kg/h, the SOE covers approximately 40% of the refinery hydrogen needs [13].

For both cases, the electrolyser module is provided by Sunfire. Its internal heat integration is depicted in

Fig. 2.1, which illustrates that the anode exhaust stream preheats the incoming air for the stack while the remaining heat requirements are provided by an external heater. The steam is first heated by the cathode exhaust and later brought to the stack temperature by an external heater.

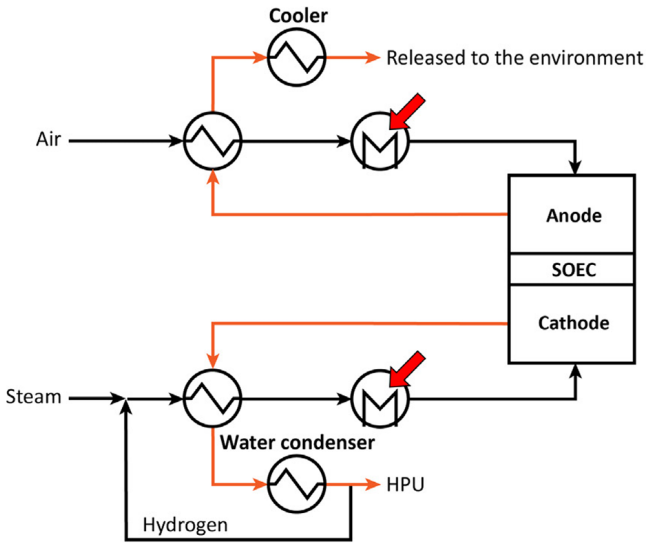

Figure 2.1: *Simplified diagram of the SOE thermal integration system developed by Sunfire, from [7].*

These two projects are, to date, the most significant in size. Besides these existing infrastructures, one can investigate the latest heat integration made in the literature.

Crespi et al. [14] study a 5KW SOEC stack integrated with a concentrated solar power (CSP) unit and thermal energy storage. The system uses high-temperature heat from a CSP source to provide the thermal input for water evaporation. In their design, the inlet flows are heated up to around 700°C. Then, to recover the heat from exhaust gases, two different preheating mechanisms are implemented. The exhaust air leaving the stack goes through a heat exchanger to preheat the inlet sweeping air. Following the preheating, the inlet air is brought to the desired stack temperature by an electric heater. On the water side line, no heat recuperation is done by outlet streams from the stack, but the water is first evaporated by a steamer fed by CSP and is afterwards heated up to around 700°C by an electrical heater.

The sole integration of a solid oxide electrolyser with a power bottoming cycle is from Wang et al. [15]. They develop a hybrid system integrating a marine diesel engine with a SOEC and ORC for hydrogen production. Electrical power required by the electrolysis is provided by the marine engine while the exhaust heat from the engine preheats the steam fed to the SOEC and afterwards, the remaining waste heat goes through an ORC to maximise energy recovery. The results indicate a system efficiency of 53.56%, which is higher than a stand-alone diesel engine. Aside from the overall system, the ORC has an efficiency of 12.12% considering a turbine inlet temperature of 277°C. The waste heat recovery for steam preheating allows the SOEC to reach an effiency of 104.41%, approximately 20% above SOEC's efficiency without external heat integration.

The other closest examples found in literature are PEM-based rather than SOEC-based. Li et al. [16] compare both an ORC and an absorption refrigeration cycle to recover waste-heat from a 100 MW PEM to reduce the energy demand of the hydrogen liquefaction process. The ORC achieves an efficiency of 10.93% with a low temperature of the PEM outlet, around 80°C. These results demonstrate that, with low-temperature waste heat, only a small fraction of the energy demand can be met through the cycle.

Another result of the same kind can be found in the study from Niknezhad et al. [17], who analyse the

heat recovery of 10 MW PEM by an ORC. With a hot source for the ORC of 76.48°C, the cycle achieves 10.13%. This result highlights again that bottoming cycles recovering heat at low temperatures struggle reaching high efficiencies.

In conclusion, no direct integration of a SOE for hydrogen production with a bottoming power cycle has ever been made in the literature. Although Wang et al. [15] investigated the integration of an ORC with a SOE stack, the motivation behind the paper is the recovery of heat from the diesel engine. However, the current project for which this work is done considers hydrogen production solely. Therefore, the heat integration made in [15] cannot be directly transposed to this work. The other novelty of this work is the use of a sCO_2 as a bottoming cycle and not an ORC. Indeed, most of the investigated works would consider an ORC for waste recovery applications.

2.2 Modification

In the current process, a total of four heat exchangers are used for heat recuperation. However, this heat exchanger network could be simplified. First, the heat duty in HX-a1 is negligible compared to the one in HX-a2. For this reason, HX-a1 is removed and HX-a2 kept. Then, HX-w1 is removed and HX-w2 kept. This simplification arises from a desire to simplify the heat recuperation and align the new design with the ones described in the previous literature review.

The new configuration, shown in Fig. 2.2 and used as the base case, contains two heat exchangers. The zone within which the heat exchangers were removed are within the green parallelogram. Stream characteristics are reported in the Appendix.

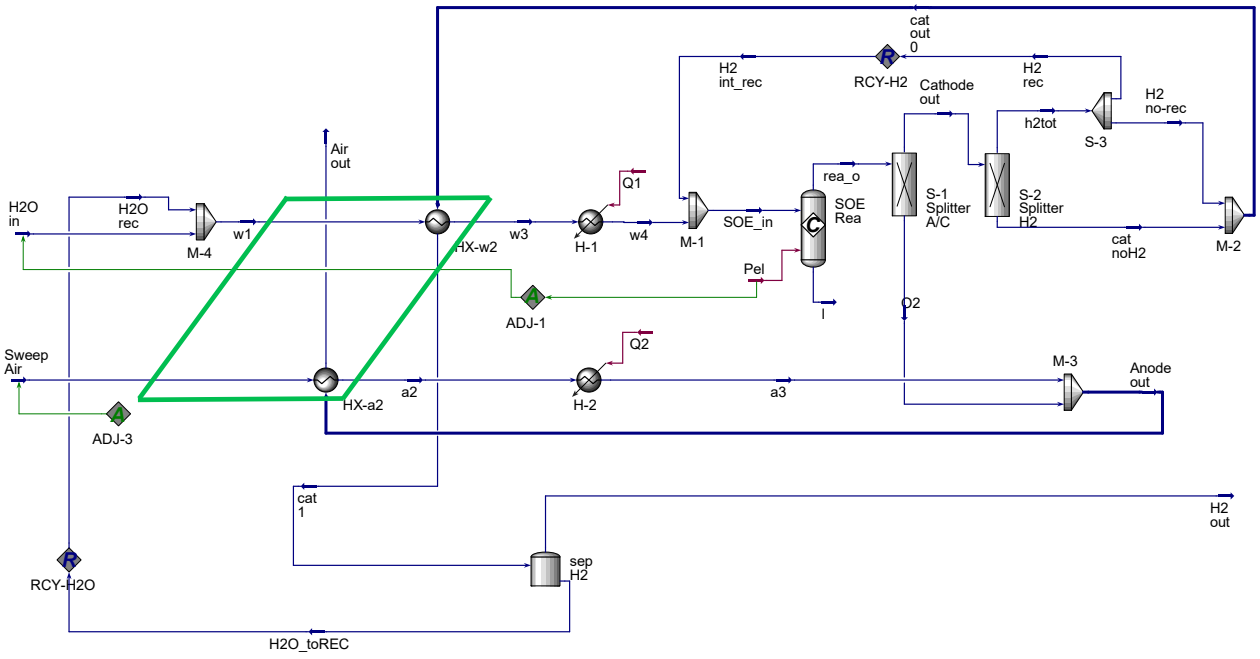

Figure 2.2: *Updated base case process flowsheet in Aspen HYSYS™.*

In Fig. 2.2, it can be seen that HX-a1 and HX-w1 have been removed. Consequently, the two types of heat exchange are air/air in HX-a2 and water/hydrogen-water in HX-w2. While the previous design imposed a fixed temperature for some streams (*Air out, a2 and cat 1*), this design considers pinch values of 20 K to ensure physical coherence. From [18], it appears that for shell-and-tube heat exchangers, typical pinch values in the chemical industry lie between 10-20K. The value of 20K is therefore taken as

a plausible one.

As the heat recuperation is lowered, the heat inputs in H-1 and H-2 are expected to increase. The comparison between the two designs is shown in Table 2.1.

Table 2.1: *Comparison between the thermal demand at the heaters between the previous and new designs.*

Thermal demand	Previous design	New design
H-1 (W)	128	990
H-2 (W)	862	109
Total (W)	990	1099

Removing the two mentioned heat exchangers leads to a relative thermal input increase in the heaters of 11%. This small difference is a result of the fact that in the previous case, temperatures were imposed. As a consequence, as seen in Fig. 1.7b, the heat exchanger HX-a2 was not optimal considering the large temperature gap between the two streams along their heat exchange. Imposing the pinch, as can be seen in Fig. 2.3a, enables the sweep air stream to be preheated to a higher temperature, further decreasing the load on the heater H-2.

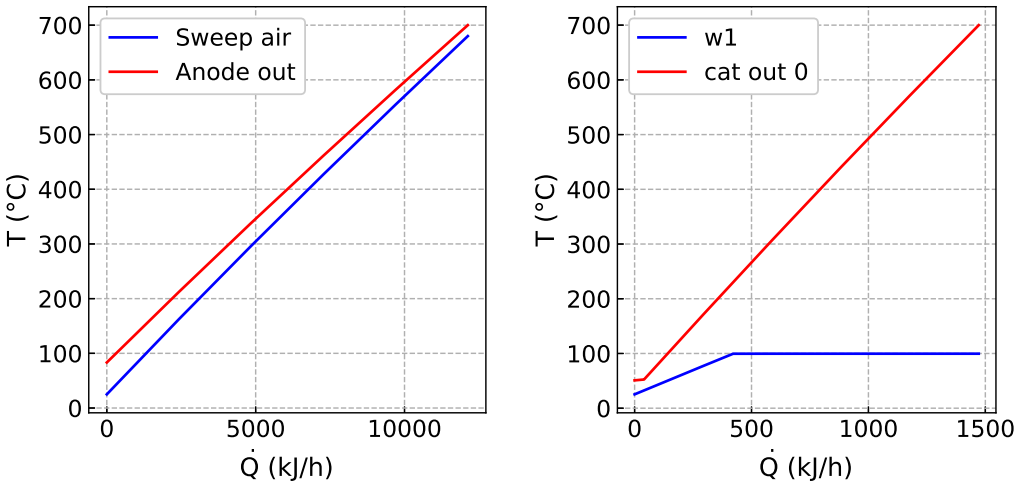

(a) *HX-a2.* **(b)** *HX-w2.*

Figure 2.3: *T-Q profiles in the heat exchangers for the new design.*

However, removing HX-w1 forces HX-w2 to evaporate the water. As demonstrated in Fig. 2.3b, the heat capacity flow rate of the hot stream is not high enough to fully evaporate the water, which leads to a less efficient heat exchanger compared to the previous case. At the outlet of HX-w2, the vapour fraction amounts to 35% of the phase mix. Consequently, the thermal input in H-2 increases to complete evaporation and superheats the steam to 700°C.

Chapter 3

Literature review for waste heat recovery

This chapter establishes the foundation for the power bottoming cycle modelled in this work. First, the different bottoming cycle technologies for high-to-medium temperature waste heat recovery (WHR) are compared, leading to the selection of supercritical CO_2 Brayton cycle (sCO_2). Then, a state of the art of sCO_2 cycles is considered. Finally, the diverse approaches for quantifying the performance of an integration are discussed.

3.1 Power cycles for WHR

The criteria for selecting the bottoming cycle layouts are derived from the methodology detailed by Astolfi et al. [19]. In the paper, they compare organic Rankine cycles (ORC) and closed-loop CO_2 cycles for the exploitation heat sources in the range 5-50 MW. At such small thermal powers, traditional steam Rankine cycles have low efficiency. The authors demonstrate that, at low heat source temperatures, cycles working with organic fluids achieve higher cycle efficiencies whereas at higher heat source temperatures, supercritical CO_2 cycles exhibit higher efficiencies.

To come up with these results, Astolfi et al. [19] simulate different ORC layouts (saturated and superheated, both with and without recuperation) and four CO_2 cycles (simple non-recuperative (SnR), simple recuperative (SR), recompressed recuperative (RR) and cascade recompressed (CR)). They subsequently carry out an optimisation with the plant efficiency as the parameter to maximise. The latter is defined as the ratio of the net cycle electrical power to a maximum recoverable heat, fixed in their optimization. The result of their work consists of maps that indicate the most efficient cycle based on the hot source temperature and the cooling grade of the heat source. The cooling grade is the ratio of the actual temperature difference under which the hot source goes through, divided by the theoretical temperature difference of the hot source outlet temperature if it was cooled down to the cold sink temperature.

As illustrated in Fig. 3.1a, sCO_2 cycles are more efficient than ORCs for heat source temperatures above approximately 350–400 °C while ORCs are more efficient below this range. It should be noted that this figure considers air as the cooling source at the gas cooler of the cycle. Water is another possible source but will not be considered as detailed further below. Figure 3.1b details optimal CO_2 cycles layouts as a function of the same axis parameters. In this work, the idea is to use the high temperature exhaust streams of the SOE to power a bottoming cycle while the remaining heat is used to preheat the inlet streams. Considering that there will be a trade-off between using the SOE exhaust heat for preheating feed streams or for powering the bottoming power cycle, the cooling grade of the hot source for the bottoming cycle is expected to be limited. For this reason, simple recuperative and recompressed recuperative cycles are selected as they are the most efficient configurations for cooling grades below 50%.

In summary, these results demonstrate the superior performance of sCO_2 cycles over ORCs for medium-to-high temperature heat sources. Considering the aim of this project to be the exploitation of 700°C exhaust streams at the SOE outlet, ORCs will not be assessed in this work since their use is restricted to low temperature, and their efficiency remains low even in those conditions.

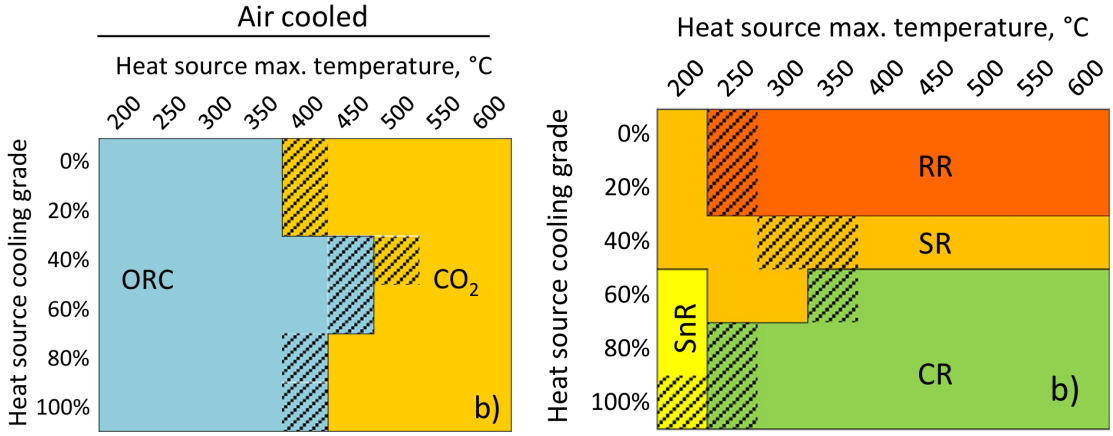

(a) *Selection map ORC vs sCO_2 for air cooled power cycles.* **(b)** *sCO_2 selection map with the four simulated cycle configurations.*

Figure 3.1: *Selection maps for low-to-high temperature heat source, from [19].*

For high temperature heat sources, Thielens et al. [20] demonstrate the superiority of supercritical carbon dioxide cycle for high temperature heat recovery. In their article, the authors aim to compare an sCO_2 cycle with a conventional steam cycle for the waste heat recovery of a waste incinerator. To achieve this comparison, they use a real-world waste incinerator utilising a steam cycle in a cogeneration setup. The steam setup in place is compared with a numerical model of a sCO_2 cycle. The results show that the sCO_2 configuration outperformed the steam cycle both in off-design and nominal operation. At nominal operation, the sCO_2 demonstrates a 7% higher cycle efficiency than its counterpart while at off-design, the mean cycle efficiency is 6% higher for the sCO_2 layout.

Still on the subject of comparing sCO_2 and steam cycles, the following study performed by Pidaparti et al. [21] provides a techno-economic analysis of using a sCO_2 cycle instead of a triple-pressure reheat steam Rankine cycle in a natural gas combined cycle plant. The authors develop three different sCO_2 configurations. At a gas turbine exhaust temperature of 596°C, it appears that all sCO_2 layouts show similar plant efficiency to the reference triple-pressure reheat steam Rankine cycle. From an economic perspective, the capital costs for sCO_2 are nearly twice that of steam Rankine cycles. However, despite these larger costs for the cycle itself, the levelised cost of electricity (LCOE) of one of the sCO_2 configurations turns out to be slightly lower than the steam counterpart, respectively of 65.7 $/MWh and 66.1 $/MWh. Finally, the study emphasizes that the sCO_2 efficiency is strongly dependent on the gas turbine exhaust temperature. At 629°C, the sCO_2 design achieves a 0.7% higher efficiency and a 1.4% lower LCOE compared to the reference steam Rankine cycle.

These two studies confirm the potential superiority of sCO_2 cycles for waste heat recovery at high temperature. The next section will also provide additional details of the benefits of using a sCO_2 cycle over a traditional triple-pressure reheat steam Rankine cycle.

3.2 State of the art of sCO_2 cycles

This section summarises relevant findings for this work on the state of the art of supercritical CO_2 Brayton cycles.

As a working fluid, carbon dioxide has several cost advantages, as it is widely available and inexpensive but also shows a safe chemical behaviour being non-toxic and non-explosive [22]. A supercritical CO_2 Brayton cycle has five main components which are a gas heater, a turbine, a recuperator, a gas cooler, and finally, a compressor. This basic configuration corresponds to a simple recuperative cycle.

Just above the critical point ($T_{crit} = 31.03°C$ and $P_{crit} = 73.8$ bar [23]) CO_2 has a liquid-like behaviour, as its density is very high at that point as displayed in Fig. 3.2. To take advantage of this, the compressor works close to critical point as it enables a low compressor work relative to the pressure ratio [24]. However, operating close to the critical point can lead to the appearance of a two-phase mixture, as the fluid is being accelerated at the leading edges of compressor blades, eventually reducing the fluid's pressure and entering the two-phase region [22].

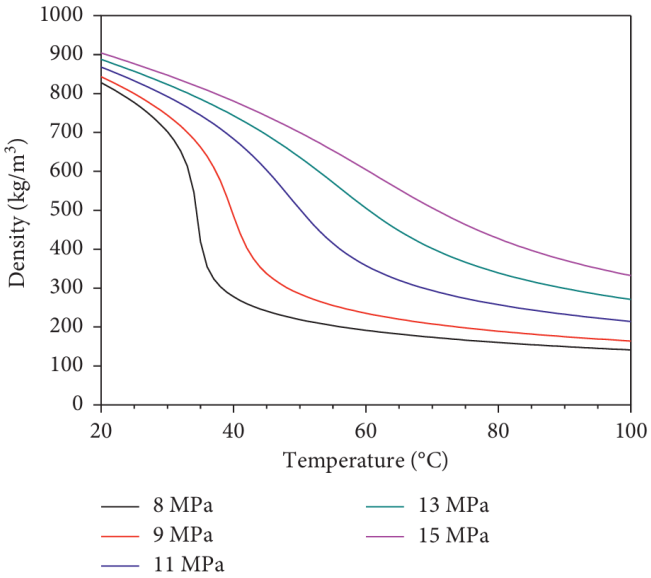

Figure 3.2: *Carbon dioxide density vs temperature for different supercritical pressures, from [25].*

Regarding the size of the components, optimisation studies came up with the optimal high pressure lying between 200 and 400 bar [24]. Therefore, the fluid's density stays high in the entire cycle, allowing the use of compact turbomachinery. For the same power output, sCO2 turbomachinery can be up to 10 times smaller than their steam Rankine cycle turbomachinery counterparts [22]: it does not only result in smaller investment costs, but also in a reduced physical footprint of the system.

Another great advantage of supercritical cycles is how the heat is exchanged at the different heat exchangers. In a subcritical cycle, the fluid phase change induces a mismatch between the temperature profile of the heat source/sink and the working fluid one. This results in further irreversibilities. In a supercritical cycle, as there is no phase change, the temperature profiles in the heat exchangers can match better, improving the efficiency of the heat recovery process. Figure 3.3 illustrates both cases.

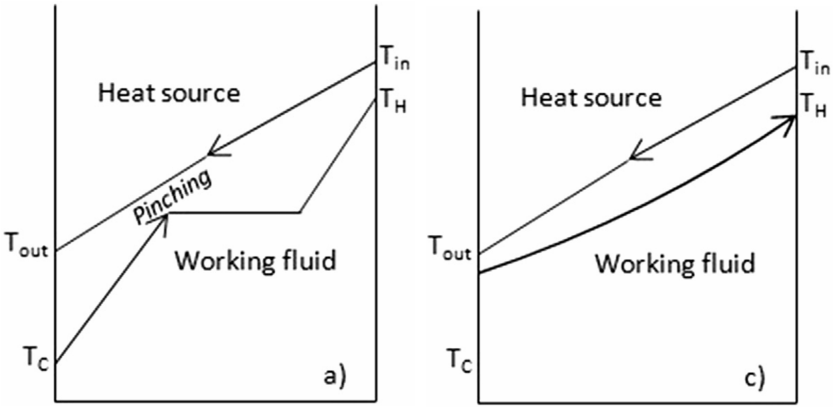

(a) *With latent heat exchange.* **(b)** *Sensible heat exchange solely.*

Figure 3.3: *Heat exchange profiles for latent and sensible heat exchanges, from [26].*

An advantage of the low critical temperature of CO_2 is that it allows cooling with ambient air. Compared to a traditional steam Rankine cycle, this removes the dependence on a water supply for the heat sink of the cycle. Let it be noted that this is valid for supercritical cycles; transcritical cycles, wherein condensation at the gas cooler occurs below the critical temperature, would require another cooling fluid [24]. For this reason, transcritical configurations will not be investigated in this work.

Despite all these advantages, supercritical CO_2 cycles still face challenges due to the high operating pressures and temperatures within the cycle. For the gas heater, microtube architecture and plate-fin structures have the characteristics to withstand extreme conditions. The problem with the conventional shell-and-tube design is the particular material required to withstand such values, increasing the cost of the system [24]. Another equipment subjected to the harsh constraints is the recuperator. This one has both low and high pressure on each of its sides. The most suitable heat exchanger types are printed circuit heat exchangers (PCHEs) [24] [22] since they have high surface area density and can resist extreme temperature and pressure. Two drawbacks come with technology: the large pressure drop they provoke in the cycle and their high cost [24]. Finally, the cooler operates at a lower pressure and temperature, making the research around its design less of a concern.

The turbine experiences the highest temperature condition considering the extreme value of the turbine inlet temperature. Below 650°C, stainless steel can be used, but above this threshold, more expensive alloys are required, causing much higher capital cost [24].

3.3 Methodologies for thermodynamic analysis

As the aim of this work is the evaluation of the integration of a bottoming cycle within a process, it is relevant to investigate the different existing approaches to assess the impact of the power cycle on the process.

Yasar et al. [27] reviewed the developments in thermodynamics methodologies. This paper is used as a guide to understand the benefits from each approach, and the most relevant ones are summarized below.

- Second Law and Exergy Analyses
  The authors explain that irreversibility in a system is proportional to the entropy production [27]. Second law analysis can be used to identify the sources of entropy production in a system by assigning an entropy generation rate $\dot{S}_{gen}$ to each component. Then, exergy analysis enables the determination of the maximum theoretical work from a certain resource. If exergy decreases, it is

because of irreversibilities. This approach can thus be used to spot the locations where irreversibilities occur. In their paper [27], the authors cite this approach to be the most used.

- Economics
  In this category, thermoeconomic and exergoeconomic analysis coexist. The first approach consists of doing a thermodynamic/exergy analysis alongside an economic analysis. The design optimum point is the one minimizing the total system cost. On the other hand, the exergoeconomic analysis assigns a monetary cost ($/J of exergy) to exergy streams. These costs are then used to evaluate the inefficiencies of the system [27].

In this work, no economic analysis will be performed because the correlations used for computing the costs of the current system lack accuracy. For instance, Sadeghi et al. [28] executed a thermoeconomic analysis for the integration of a sCO_2 cycle with a solid oxide fuel cell (SOFC). The problem comes from the origin of the correlations used to calculate the purchased costs of equipment. Indeed, these correlations are from this book [29], which dates from 1996.

Chapter 4

Cycle modelling

In this chapter, two different cycle configurations are modelled: a simple recuperative sCO_2 layout and a recompressed recuperative sCO_2 one. First, assumptions are made for all cycles. Then, each cycle is detailed by equations and afterwards validated by literature. It should be noted that this chapter does not yet consider the hot/cold source types, as the cycle integration is done in the next chapter.

4.1 Assumptions

The next assumptions are made for all cycles:

- Variation in kinetic and potential energies is negligible;
- Steady-state operation;
- Pressure drops neglected [30];
- Turbomachinery component operation is defined according to isentropic efficiencies;
- Component ambient thermal loss neglected;
- Ambient temperature T_0 of 20 °C.

For the simulation of the different cycles, the software EES from F-Chart is used. To calculate the properties of carbon dioxide, the equation of state used by the software is the Span-Wagner's model. It provides high accuracy thermodynamic properties up to 826 °C and 800 MPa [31].

4.2 Simple recuperative

4.2.1 Cycle description

The simple recuperative layout contains five elements: the compressor, the recuperator, the primary heat exchanger (PHE), the turbine and the heat rejection unit (HRU). Both cycle T-s and block diagrams are illustrated in Fig. 4.1.

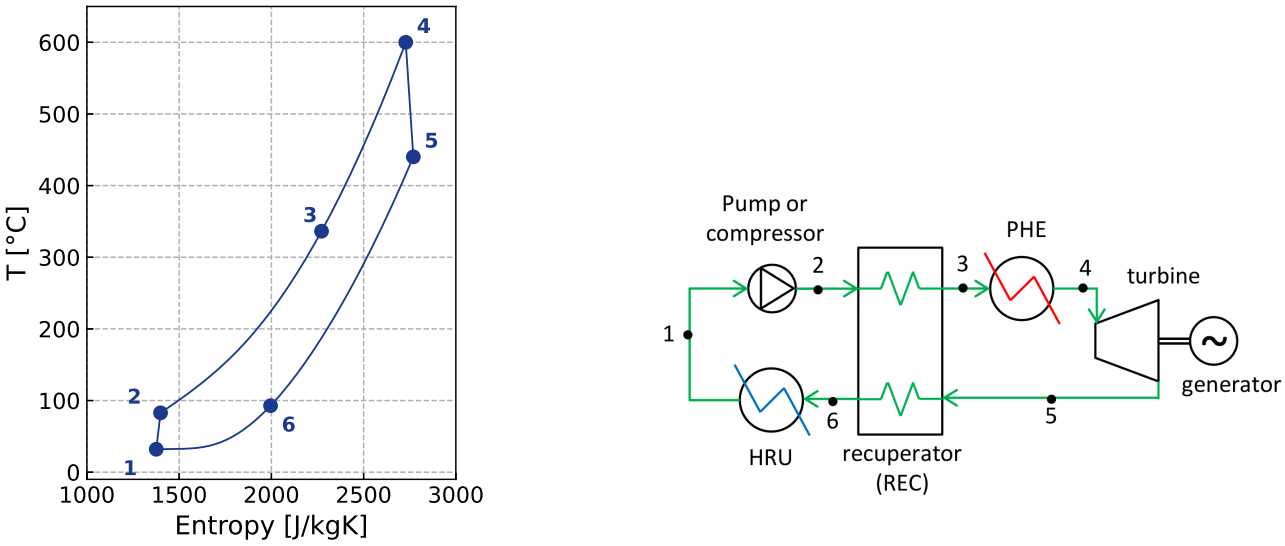

(a) *T-s diagram.* **(b)** *Cycle block diagram [19].*

Figure 4.1: *Simple recuperative cycle configuration.*

State 1 of the cycle corresponds to the inlet of the compressor, just above the critical point of the CO_2. It must be noted that the terminology compressor is employed and not pump, as the latter is utilised for fluids in liquid state. The fluid is therefore compressed to the high pressure of the cycle, $1 \rightarrow 2$. From $2 \rightarrow 3$, the fluid goes through the high pressure side of the recuperator to recover heat from the turbine outlet. Between 3 and 4, the fluid exchanges heat with the hot source through the PHE. After this heat exchange, the fluid expands in the turbine to produce work, $4 \rightarrow 5$. From 5 to 6, the fluid cools down as it goes through the recuperator low pressure side. Finally, between 6 and 1, the fluid is cooled by the cold source through the HRU.

4.2.2 Input conditions

As stated in Section 3.2, CO_2 has high density just above its critical point (31.03°C,73.8 bar). To minimise compression work, inlet compressor conditions are fixed at 32°C and 76 bar. The isentropic efficiencies are selected according to a paper from Eun-Cha et al [32]. The authors designed a 500 kW simple recuperative supercritical CO_2 cycle, with compressor and turbine isentropic efficiencies of respectively 0.80 and 0.86. As the targeted reference for this work is a 1 MW electrolyser, hundreds of kW would approximately be on the order of the potential power cycle bottoming the electrolyser. Finally, the PPTD at the recuperator is fixed at 10°C. All inputs are reported in Table 4.1.

Table 4.1: *Input parameters for the simple recuperative configuration.*

Input parameters	Value
Compressor isentropic efficiency	0.80
Turbine isentropic efficiency	0.86
$PPTD_{REC}$ (°C)	10
Inlet compressor temperature (°C)	32
Low pressure (MPa)	7.6

Two remaining parameters have to be fixed: the high temperature and high pressure of the cycle. In the

scope of model validation, the former will be fixed according to the reference it is compared to. However, when the cycle is integrated in the SOE process with a hot source, this temperature will be fixed by the PPTD imposed at the PHE. The high pressure will be analysed after in Section 4.2.4. The different inputs, outputs and parameters are illustrated through the black-box diagram represented in Fig. 4.2.

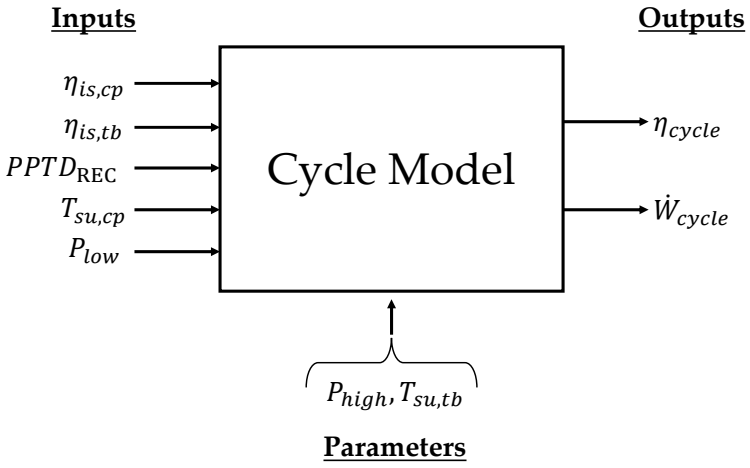

Figure 4.2: *Black-box diagram for the simple recuperative cycle model.*

4.2.3 Modelling

The compressor is characterised by an isentropic efficiency. As the temperature and pressure are known at the compressor's inlet, the state of the fluid can be calculated (h_1, s_1). Following the definition of the isentropic efficiency, the enthalpy at the compressor's outlet is computed:

$$\eta_{is,cp} = \frac{h_{2,is} - h_1}{h_2 - h_1} \tag{4.1}$$

where $h_{2,is} = f(P_2, s_1)$. The power input at the compressor can then be calculated,

$$\dot{W}_{cp} = \dot{m}_{\mathrm{CO_2}} \cdot (h_2 - h_1) \tag{4.2}$$

To model a heat exchanger, such as the recuperator, different approaches exist:

- Effectiveness based on temperature difference:

$$\epsilon_{REC} = (T_5 - T_6)/(T_5 - T_2) \tag{4.3}$$

- Effectiveness based on enthalpy difference:

$$\epsilon_{REC} = (h_5 - h_6)/(h_5 - h(P_6, T_2)) \tag{4.4}$$

- Pinch analysis method

The first method views the heat capacity as constant on the considered temperature range and to be the same for both temperature differences. However, as it can be seen in Figure 4.3, CO_2 heat capacity cannot be viewed as constant, as it can vary significantly, especially near the critical point. The second approach relative to enthalpies amounts to considering temperatures with variable specific heat.

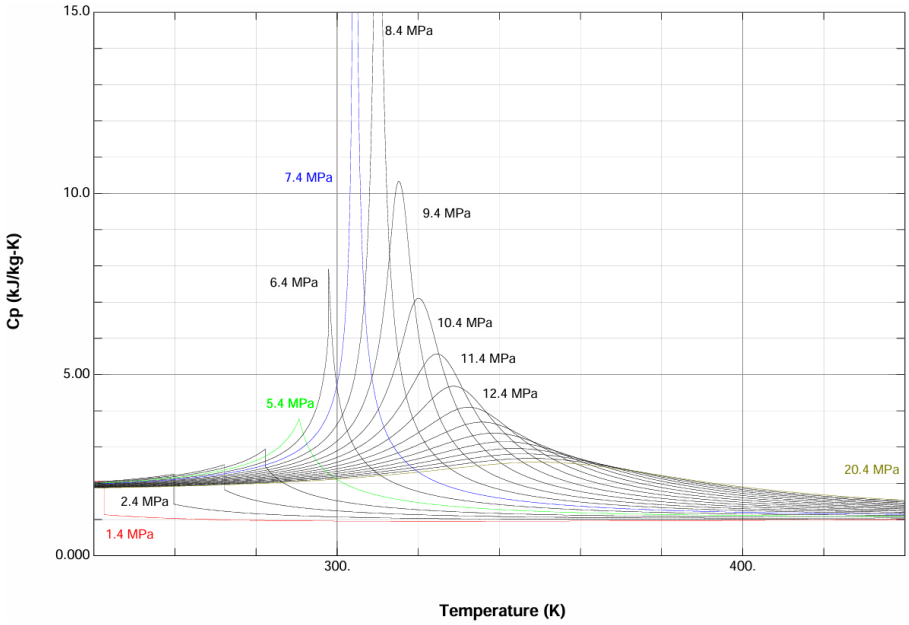

Figure 4.3: *Specific heat vs Temperature at various pressures for carbon dioxide, from [33].*

A study from Xing et al [34] compare the three different approaches in the modelling of a supercritical CO_2 cycle. The results demonstrates first that using a temperature difference based effectiveness is unsuitable for sCO_2, as it grossly overestimates the cycle's thermal efficiency. Although the enthalpy based effectiveness proved to be more accurate, it only considers inlets and outlets of the heat exchanger. This problem leads to a possibility of temperature crossover for fluids like CO_2 whose heat capacity can vary drastically.

The pinch analysis method consists of imposing a pinch point temperature difference to ensure no temperature crossover occurs within the heat exchanger. This methodology requires a discretised model of the heat exchanger and is thus more computationally demanding [34]. In this work, pinch analysis is implemented for all heat exchangers.

Considering the extreme variation of the heat capacity near the critical point where the HRU works, and the less important variation for higher temperatures and pressure, where the PHE works, that pinch analysis is evidently more relevant for the HRU than for the PHE.

As shown in Figure 4.4, a heat exchanger can be discretised in N elements with k going from 0 to N and by denoting T^k_{hot} and T^k_{cold} respectively as the hot and cold temperatures at element k.

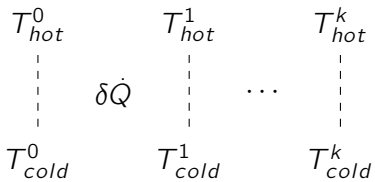

Figure 4.4: *Discretised model of heat exchanger.*

Assuming the total heat power exchanged $\dot{Q}_{tot}$, the energy balance on a slice is:

$$\dot{Q}_k = \dot{Q}_{k-1} + \delta\dot{Q} \qquad \text{with} \quad \delta\dot{Q} = \frac{\dot{Q}_{tot}}{N} \tag{4.5}$$

For each slice, both streams satisfy:

$$\dot{Q}_k = \dot{m}_{hot} \cdot (h_{hot,k} - h_{hot,0}) \tag{4.6}$$

$$\dot{Q}_k = \dot{m}_{cold} \cdot (h_{cold,k} - h_{cold,0}) \tag{4.7}$$

Where $\dot{m}_{hot}$ and $\dot{m}_{cold}$ are respectively the mass flow rates on the hot and cold sides. $h_{hot,k}$ and $h_{cold,k}$ denote the specific enthalpy at the node k.

The temperature difference is computed for each increment:

$$\Delta T_k = T_{hot,k} - T_{cold,k} \tag{4.8}$$

It enables the imposition of a pinch point temperature difference inside the heat exchanger. The system becomes constrained such that:

$$PPTD = min(\Delta T_0, ..., \Delta T_N) \tag{4.9}$$

Solving the three exchanger models, the turbine inlet characteristics are known (h_4,s_4). From the turbine isentropic efficiency, the enthalpy at the turbine's outlet is calculated:

$$\eta_{is,tb} = \frac{h_4 - h_5}{h_4 - h_{5,is}} \tag{4.10}$$

Where $h_{5,is} = f(P_{low}, s_4)$. The outlet state being fully described (h_5,P_{low}), the turbine power output is:

$$\dot{W}_{tb} = \dot{m}_{CO_2} \cdot (h_4 - h_5) \tag{4.11}$$

Finally, the cycle thermal efficiency is calculated:

$$\eta_{\text{cycle}} = \frac{\dot{W}_{\text{cycle}}}{\dot{Q}_{\text{PHE}}} \tag{4.12}$$

Where $\dot{W}_{\text{cycle}} = \dot{W}_{\text{tb}} - \dot{W}_{\text{cp}}$.

4.2.4 High pressure determination

To determine the high pressure, the pressure ratio (PR), defined as the ratio of high pressure to low pressure, is varied between 2 and 6 for a turbine inlet temperature of 680°C. The turbine inlet temperature is fixed here to determine an optimal pressure ratio; in the next chapter, this temperature will be set indirectly by the PPTD at the PHE. The value 680°C has been chosen, as it is the value of the turbine inlet temperature when the cycle is integrated as a bottoming cycle.

As shown in Fig. 4.5, the cycle efficiency is an increasing function on the considered range. For a PR between 2 and 4, the cycle efficiency significantly increases. After 4, it keeps rising, albeit more slowly.

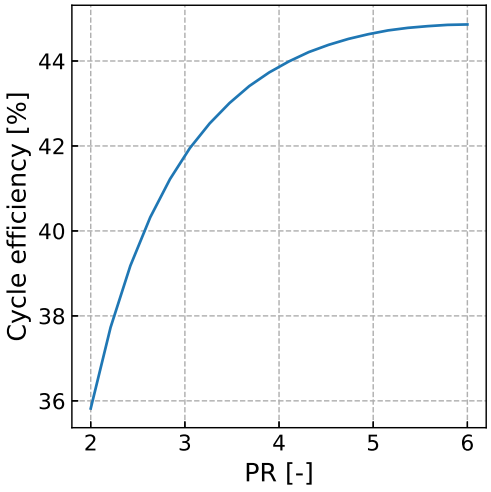

Figure 4.5: *Cycle efficiency as a function of pressure ratio.*

Among existing sCO_2 designs, a high pressure of 300 bar is an upper practical bound, with some experimental work testing a high pressure of 423 bar [24]. In this work, the high pressure for the simple recuperative design is fixed to 300 bar, which corresponds to a pressure ratio of 3.95.

4.2.5 Model validation

To validate the model, results are validated with findings by White [35]. The author simulate the same configuration. Moreover, in his work, the recuperator is modelled as well with a PPTD. Input parameters are matched with his model's parameters shown in Table 4.2 in order to validate the equations.

Table 4.2: *Parameters used by the reference work [35] for the design of a simple recuperative sCO_2 cycle.*

Parameter	Value
Turbine inlet temperature	704.44°C
Compressor inlet temperature	35
Compressor isentropic efficiency	1
Turbine isentropic efficiency	1
$PPTD_{REC}$	10°C

The results are displayed in Table 4.3. With a relative error of 1.8%, it can be concluded that the model is validated. Such high efficiencies are too optimistic considering the unitary isentropic efficiency used for the compressor and turbine in the reference.

Table 4.3: *Comparison between cycle efficiency in the present work and the reference [35].*

η_{cycle}	η_{cycle} from [35]	Rel. error
51.54%	52.5%	1.8%

4.3 Recompressed Recuperative

The motivation for the use of a recompressed recuperative cycle stems from an incompatibility of heat capacity rates at the recuperator. In the previous cycle, the recuperation is limited by the heat capacity

rate on the cold side. Indeed, from Fig. 4.3, when operating in the supercritical range, it can be seen that at low pressure, the specific heat capacity of carbon dioxide significantly increases when getting close to the critical point temperature.

Depicted in Fig. 4.6, as the temperature of the cold fluid decreases, its heat capacity increases. As a result, the temperature on the cold side varies more slowly than the temperature on the hot side. The PPTD value being imposed forces the PPTD at the cold side inlet. To solve this problem and improve recuperation, namely to increase PHE's inlet temperature or decrease HRU's inlet temperature, a recompression stage is implemented and recuperation is divided in two steps.

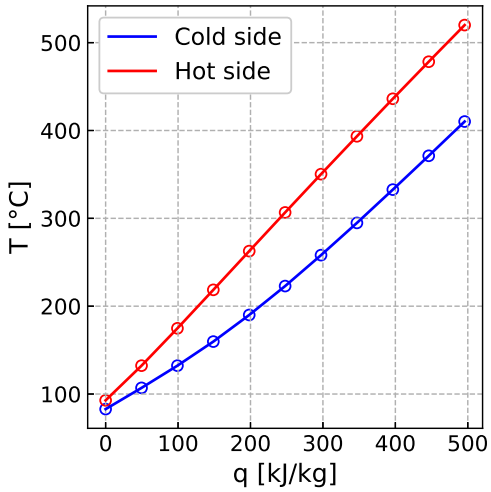

Figure 4.6: *T-q profile in the recuperator for the simple recuperative cycle.*

4.3.1 Cycle description

As illustrated in Fig. 4.7b, a recompressor and a recuperator are added to the cycle compared to the previous design.

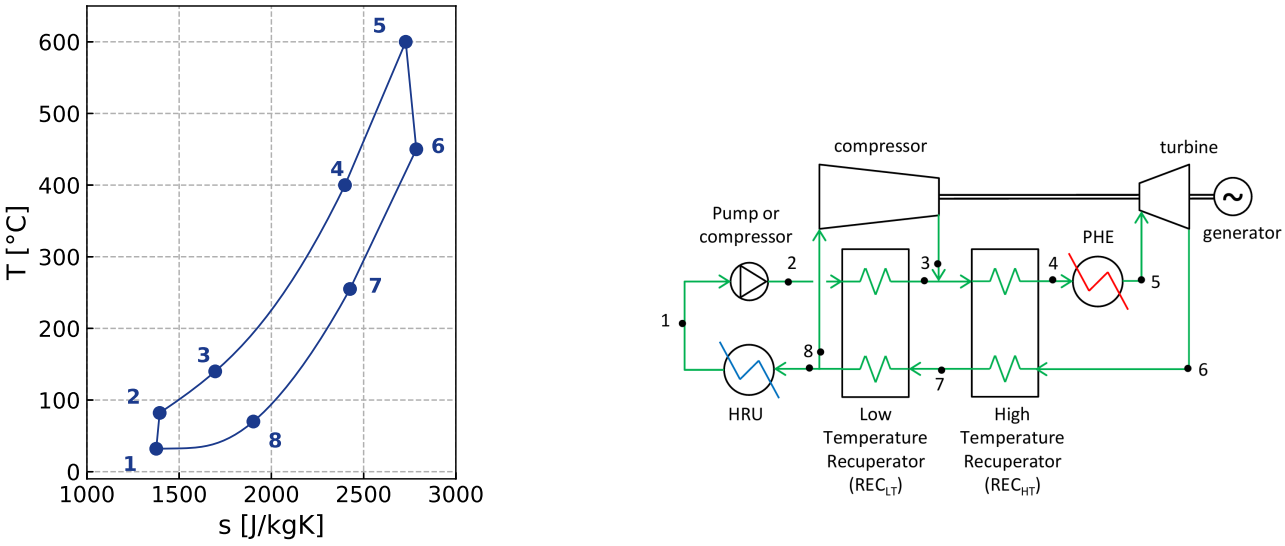

(a) *T-s diagram.*

(b) *Cycle block diagram [19].*

Figure 4.7: *Recompressed recuperative cycle configuration.*

At the turbine outlet, the total mass flow rate exchanges heat through the high temperature recuperator (HTR) where the mass flow rate is the same on both sides of the exchanger. Subsequently, the flow rate on the hot side transfers heat through a low temperature recuperator (LTR) with a reduced portion of the total mass flow rate on the LTR cold side. Indeed, at the LTR outlet on the hot side, a portion x of the flow is sent to the recompressor. Therefore, the mass flow rate on both sides of the LTR is not the same. It enables a better match of the heat capacity rates, as reducing the mass flow rate on the cold side of the recuperator counterbalances the previously discussed limiting phenomenon of the higher heat capacity at lower temperature. This will be highlighted in a further subsection.

As a consequence of this split, a fraction x of the fluid is not cooled by the HRU but directly pressurised to the cycle high pressure by the recompressor. The remaining (1-x) fraction is cooled by the HRU, to then be compressed by the main compressor and go through the LTR. Finally, the two streams are mixed before the HTR.

4.3.2 Updated inputs and equations

Regarding the different heat exchangers, the discretised model for the HRU changes due to the fraction x not being cooled while the model for the PHE remains the same. The HTR's model is the same as the previous cycle recuperator. However, the LTR is not implemented as before, as the cold side mass flow rate is a fraction of the hot side. The recompressor's isentropic efficiency is set to the same value as that of the main compressor. As before, the turbine inlet temperature is set to 680°C. Table 4.4 summarises the updated input parameters.

Table 4.4: *Fixed input parameters for the recompressed recuperative configuration.*

Fixed input parameters	Value
Compressor isentropic efficiency	0.80
Recompressor isentropic efficiency	0.80
Turbine isentropic efficiency	0.86
$PPTD_{LTR}$ (°C)	10
$PPTD_{HTR}$ (°C)	15
Inlet compressor temperature (°C)	32
Low pressure (MPa)	7.6

Finally, the black-box diagram is updated and shown in Fig. 4.8.

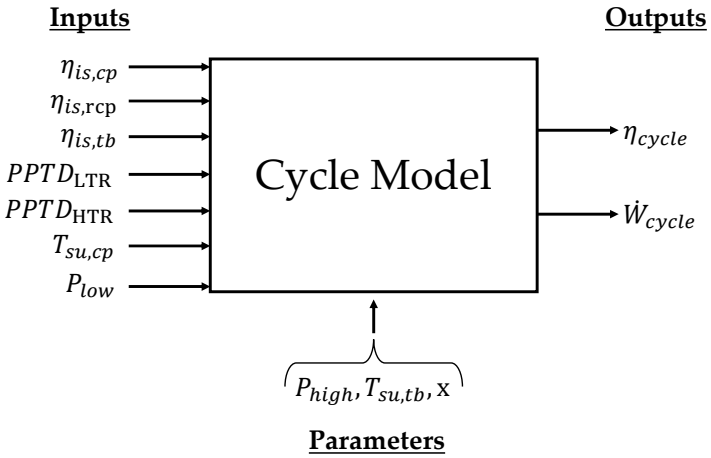

Figure 4.8: *Black-box diagram for the recompressed recuperative cycle model.*

Besides heat exchangers, compressors are updated, and the mixing point equation is added to close the system. The expression for the main compressor becomes:

$$\dot{W}_{mc} = (1 - x) \cdot \dot{m}_{wf} \cdot (h_2 - h_1) \tag{4.13}$$

Denoting 8' as the state of fluid after the recompressor, the recompressor power is:

$$\dot{W}_{rcp} = x \cdot \dot{m}_{wf} \cdot (h_{8'} - h_8) \tag{4.14}$$

Denoting states 2' and 3, respectively, as the fluid conditions at the high-pressure side outlet of the LTR and after mixing, the energy balance at the mixing point is:

$$(1 - x) \cdot \dot{m}_{wf} \cdot h_{2'} + x \cdot \dot{m}_{wf} \cdot h_{8'} = \dot{m}_{wf} \cdot h_3 \tag{4.15}$$

Finally, the net power output is updated:

$$\dot{W}_{cycle} = \dot{W}_{tb} - \dot{W}_{mc} - \dot{W}_{rcp} \tag{4.16}$$

4.3.3 Optimisation of pressure and split ratios

PPTDs and isentropic efficiencies being fixed, two independent variables remain unset: the pressure ratio PR and the split ratio x. To evaluate the impact of these variables on the cycle thermal efficiency, both parameters are varied. The pressure ratio will be varied between 2 and 4, the latter corresponding to a high pressure of around 30 bar. The split ratio variation range is set to 0.2-0.5. Fig. 4.9 shows the results.

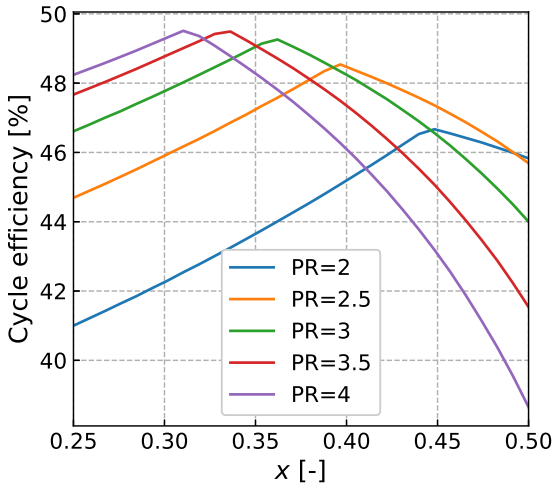

Figure 4.9: *Cycle thermal efficiency as a function of split ratio for different pressure ratios.*

As shown in Fig. 4.9, there is an optimal split ratio that maximises the cycle's efficiency for each pressure ratio. This behaviour can be explained through the T-q diagram in the LTR. Let it be known that, in the work from Kim et al [36] the same diagram as Fig. 4.9 is produced. However, their optimal split ratio is around 0.3 while in this work, it is around 0.33. In their paper, this figure was modelled with an enthalpy-based effectiveness for the recuperators, whereas pinch analysis is used in the present work.

Fig. 4.10 shows a temperature profile for two different cases for a fixed pressure ratio, fixed to 3.5 in this case. Fig. 4.10a corresponds to the case where the cycle efficiency is not maximised while Fig. 4.10b corresponds to the case where the split ratio value of 0.34 maximises cycle efficiency. On the left figure, there is a slight imbalance between the slopes of the curves, leading to irreversibilities. In the right figure

however, there is a better matching between the two curves, decreasing the irreversibilities, and therefore explaining the higher cycle efficiency. This occurs when the heat capacity rates of the hot and cold flow are identical [36]. Indeed, when x increases or decreases compared to the optimum, the heat capacity rate on the cold side of the LTR is modified, and leads to unbalanced heat capacity rates on either sides of the LTR.

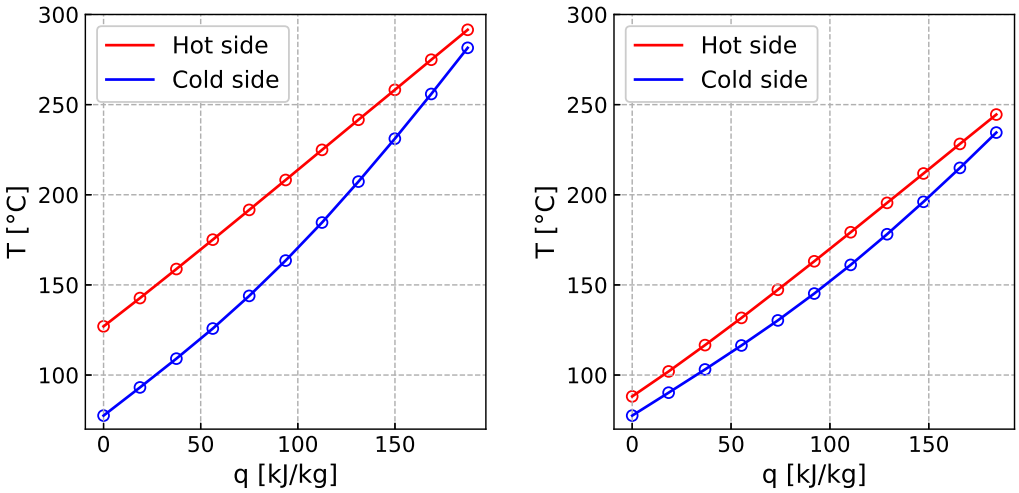

(a) *Non-optimal case (with x=0.45).* **(b)** *Optimal case (with x=0.34).*

Figure 4.10: *T-q profiles in the LTR for a pressure ratio of 3.5.*

Another aspect to discuss is how the optimal split ratio varies with the pressure ratio. As discussed before, above the critical pressure, the heat capacity decreases with increasing pressure. Fig.4.9 illustrates that, as the pressure ratio rises, the optimal split ratio diminishes and the optimal efficiency increases. As a result of decreasing the split ratio, a higher mass flow rate goes through the LTR side. This effect counterbalances the decrease of the heat capacity because of the higher pressure.

Finally, the impact of the pressure ratio on the maximum cycle efficiency can be studied. For each pressure ratio, the split ratio is varied and the maximum cycle efficiency is retrieved. Fig. 4.11 displays the maximum achievable cycle efficiency and corresponding specific work in the different equipments for different pressure ratios.

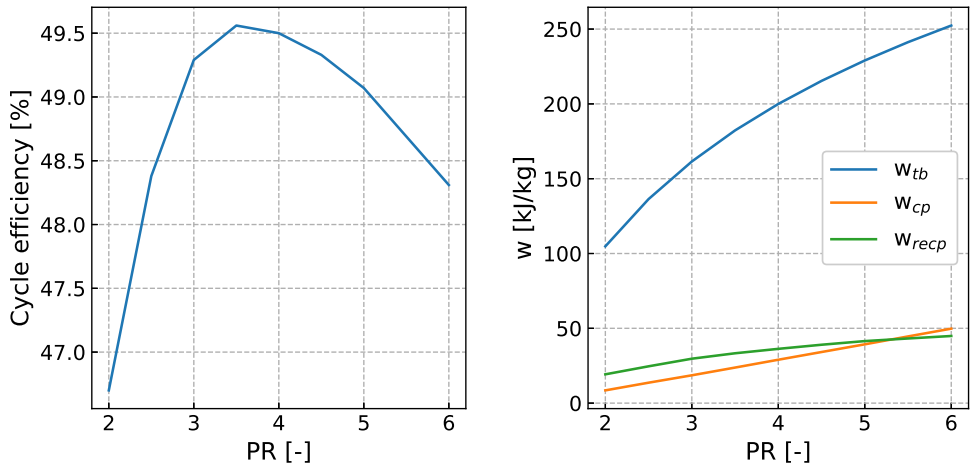

(a) *Cycle thermal efficiency.* **(b)** *Optimal specific works.*

Figure 4.11: *Optimal cycle characteristics as a function of the pressure ratio.*

Unlike the simple recuperative cycle where the efficiency keeps increasing with the pressure ratio, the latter reaches a maximum for the optimum efficiency of the cycle. From a pressure ratio of 3.5, the work in the compressor increases proportionally more than the turbine work.

4.3.4 Model validation

To validate the model, the paper from Kim et al. [36] is used as a reference. The authors optimise the cycle for different sets of PPTDs in the LTR and HTR.

Table 4.5: *Comparison of cycle efficiencies with reference [36] for different PPTDs.*

$PPTD_{LTR}$ [°C]	$PPTD_{HTR}$ [°C]	η_{cycle} [%]	η_{cycle} [%] from [36]	Rel. error [%]
10	15	43.38	44.10	1.6
10	20	43.06	43.80	1.7

Considering the relative errors computed above, one can assume that the recompressed model in this work is validated.

Chapter 5

Cycle integration with SOEC

This chapter first establishes the location at which the bottoming power cycle is placed. Then, the simple recuperative and recompressed recuperative configurations developed in the previous chapter are compared as a function of the thermal power given to them. Finally, different approaches for assessing the impact of the integration are investigated to determine the benefit from the bottoming cycle.

5.1 Cycle integration

To integrate the bottoming cycle modelled with EES, the cycle's PHE is modelled by a cooler unit in Aspen HYSYS™. Simulation results are then retrieved from Aspen HYSYS™ to EES.

5.1.1 Location of integration

To take advantage of the high efficiency of sCO_2 cycles at high temperatures, the bottoming cycle can be put at locations in the process where the temperature is the highest. In this case, the highest temperature of 700°C occurs at both outlets of the electrolysis cell, that is the anode and cathode outputs.

In the following paragraph the issues related to a bottoming cycle place on the cathode output are reported. First, as discussed in Section 1.2, the heat capacity rate is approximately 10 times lower on the cathode side compared to the anode one. The second issue is the highly flammable nature of hydrogen. Indeed, hydrogen has a wide flammability range in the air (4-75%) and very low minimum ignition energy from 0.02 mJ [37]. Therefore, any leak of hydrogen from a heat exchanger on the cathode stream would present high fire risks. If the integration would need to be done anyway, for safety reasons, the hydrogen stream would need to be isolated from the bottoming cycle via an intermediate heat transfer loop. However, such a loop would introduce two additional pinches because of the two heat exchangers. It would therefore reduce the temperature available for the primary heat exchanger of the bottoming cycle. Considering these issues, the bottoming cycle is placed on the anode output as evident in Fig. 5.1. The simple recuperative is represented for sake of simplicity.

Contrary to waste heat recovery processes where exhaust streams are not used for preheating inlet feed streams, the exhaust air stream heat can be used either to preheat the inlet sweep air stream or power the bottoming cycle. On the one hand, increasing the heat given to the cycle will produce electricity and thus decrease the net power electrical consumption by the SOE stack. On the other hand, as less heat is available to preheat the feed streams, the thermal input at the heaters H-1 and H-2 must increase as the stack temperature of 700°C must be reached in any case.

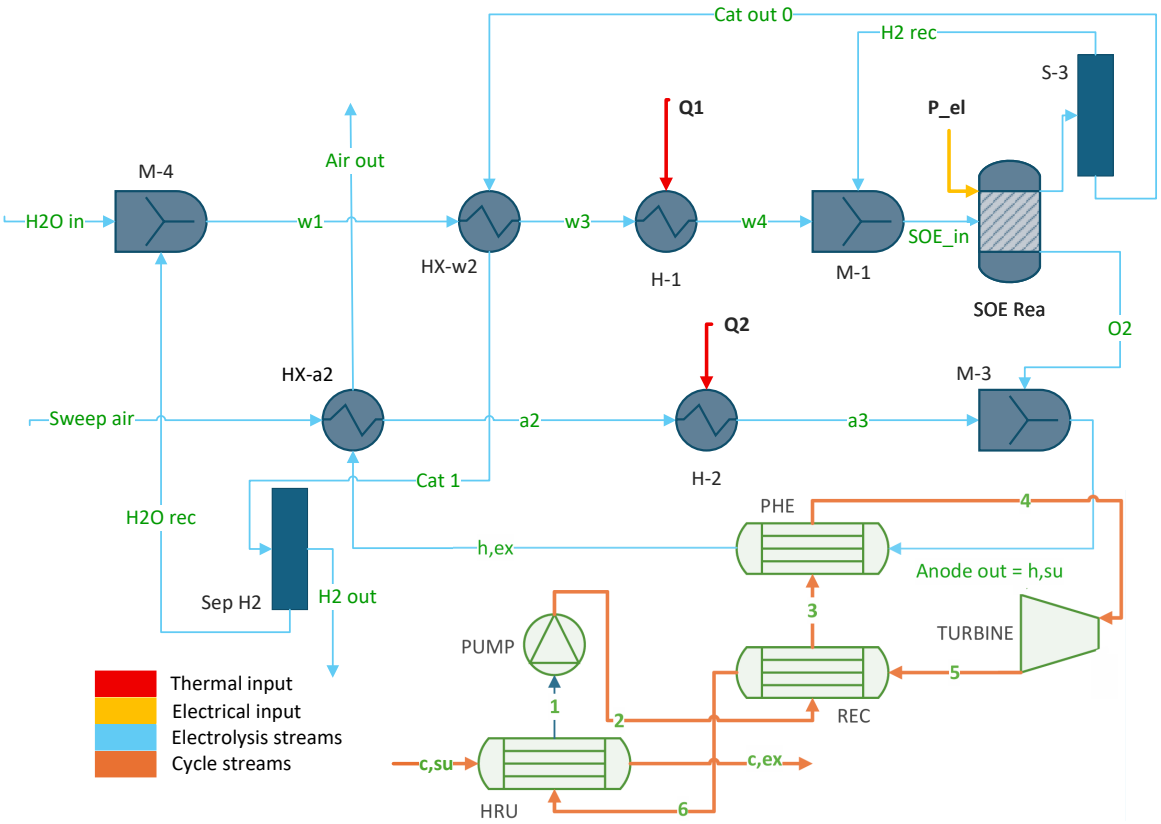

Figure 5.1: *Block diagram of the process integrated with the bottoming cycle.*

As the hot source for the cycle is the outlet air stream from the SOEC (*Anode out*), its characteristics are known and reported in Table 5.1. The cold source is considered to be air at the ambient temperature of 20°C.

Table 5.1: *Hot and cold source characteristics.*

	Hot source	Cold source
Temperature (°C)	700	20
Composition (-)	25% O - 75% N	Air
Flow rate (kg/h)	18.18	-

At this stage, the cooling degree of the hot source is unknown. Therefore, to take into account the potentially large temperature variation of the hot source fluid through the PHE, as well as the fact that the hot fluid is not stoichiometric air (since the stream is a mixture of the oxygen produced by the electrolyser and the sweep air), the expression for the mixture heat capacity is determined.
From [38], the molar heat capacity has the parametric form

$$C_p = A + B \cdot t + C \cdot t^2 + D \cdot t^3 + E/t^2 \quad (\mathrm{J/mol \cdot K}) \tag{5.1}$$

where t = temperature (K)/1000. Equation 5.1 is then evaluated with the respective coefficients from Table 5.2 to end up with expressions for the molar heat capacity of oxygen and nitrogen, $C_{p,O}$ and $C_{p,N}$.

Table 5.2: *Molar heat capacity coefficients for oxygen and nitrogen [38].*

	A	B	C	D	E
Oxygen (100 < T < 700 K)	31.32234	-20.23531	57.86644	-36.50624	-0.007374
Oxygen (700 < T < 2000 K)	30.03235	8.772972	-3.988133	0.788313	-0.741599
Nitrogen	19.50583	19.88705	-8.598535	1.369784	-0.527601

Considering the molar fractions of oxygen and nitrogen of respectively 0.25 and 0.75, the stream molar heat capacity is such that:

$$C_p = 0.25 \cdot C_{p,O} + 0.75 \cdot C_{p,N} \tag{5.2}$$

Finally, to get the value in $(J/kg \cdot K)$, the expression is divided by the mixture's molar mass.

5.1.2 Comparison between the two cycles

The cooling degree under which the hot source will go remains unknown. In other words, the thermal power given to cycle is the variable parameter. This subsection aims to compare the two cycle layouts as a function of the hot-source outlet temperature after passing through the cycle.

The discretised heat exchanger model developed is implemented for both PHE and HRU units. Table 5.3 explicits the PPTDs for each cycle configuration.

Table 5.3: *Pinch-point temperature difference across heat exchangers for each cycle configuration.*

Heat exchanger	Simple Rec., PPTD (°C)	Recompressed Rec., PPTD (°C)
Primary heat exchanger	20	20
Heat rejection unit	10	10
Recuperator	10	–
Low temperature recuperator	–	10
High temperature recuperator	–	15

Before comparing the two cycle configurations, the concept of cooling grade is detailed here. It is defined as:

$$\text{Cooling Grade} = \frac{T_{h,su} - T_{h,ex}}{T_{h,su} - T_0} \tag{5.3}$$

It represents the ratio of the temperature difference at the hot source to the temperature difference if the hot source was cooled down to ambient temperature. To better understand this concept, Fig. 5.2 illustrates cases for two different cooling grade values.

By comparing the two subfigures, Fig. 5.2 demonstrates that the temperature profile of the cold source does not vary between the two scenarios. The PPTD at the recuperator is between states 2 and 6 for both cases. Since states 1 and 6 do not change between the two cases, the PPTD in the HRU occurs at the same location regardless of the cooling grade. On the other hand, the PPTD at the PHE shifts between the two cases.

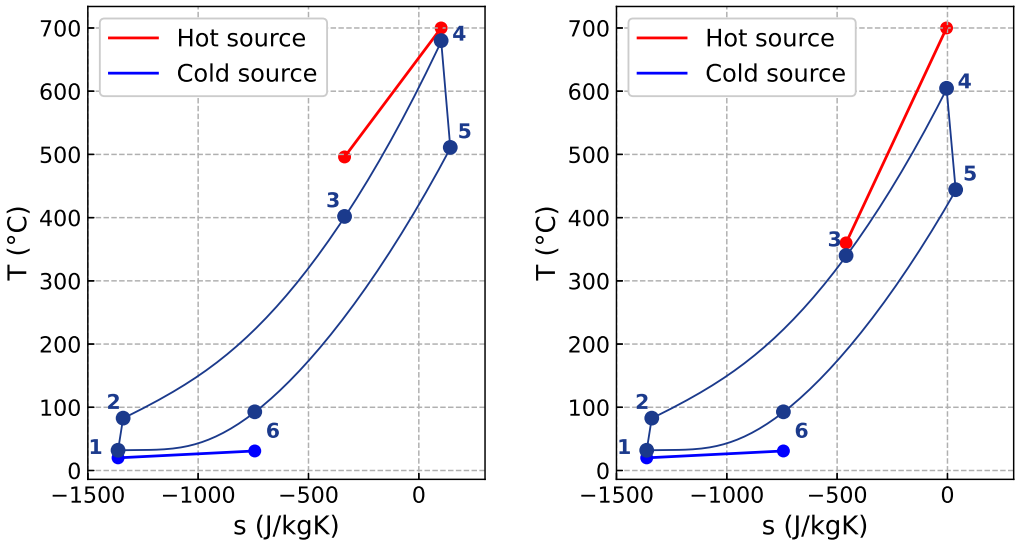

(a) *30% hot source cooling grade.* **(b)** *50% hot source cooling grade.*

Figure 5.2: *T-s diagrams for the simple recuperative case with two different hot source cooling grades.*

The integration and the concept of cooling grade being fully defined, the two cycles can be compared as a function of the hot source cooling grade.

Before analysing Fig. 5.3, it should be noted that each simulated point for the recompressed configuration maximised the cycle efficiency by varying the split ratio and pressure ratio at the same time. This was done through the use of the Min/Max function in EES.

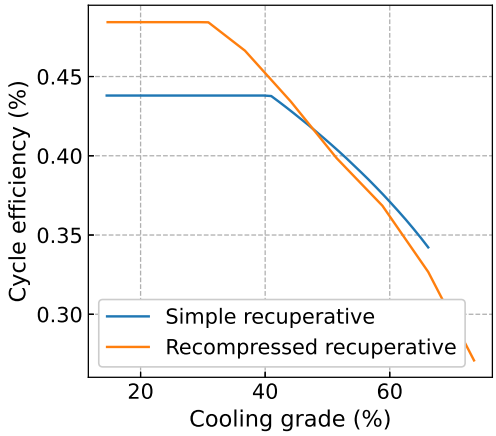

Figure 5.3: *Cycle efficiency as a function of the cooling grade for both cycle configurations.*

For low cooling grade, it appears in Fig. 5.3 that the recompressed layout is more efficient than the simple one. This superior efficiency is a result of the better matching of the heat capacity rates as discussed before in Section 4.3. Then, as the cooling grade increases, the cycle efficiency decreases for both cycles. This is because the high temperature (the turbine inlet temperature) of the cycle changes position. This can be viewed in Fig. 5.2. For low cooling grade, the PPTD is at the turbine inlet. However, as the cooling grade increases, the hot source outlet temperature decreases such that at some point, the PPTD is located at the hot source outlet temperature. This results in a decrease of the turbine inlet temperature, and thus a decrease of the cycle efficiency. One last phenomenon can be noticed. For high cooling grades,

the simple recuperative configuration is more efficient than the recompressed one, which is confirmed by the work from Astolfi et al. [19]. They discover that the recompressed recuperative cycle is more efficient than the simple one for cooling grades below 40%. In this work, the threshold arises around 47%.

5.2 Exergy analysis

A first approach to assess the impact and potential benefits from a bottoming cycle in the current process is through an exergy analysis. Exergy is the maximum theoretical work a stream can deliver if this stream is used to run a Carnot machine until it reaches environment conditions [29]. Exergy is therefore a measure of the quality of a stream, as a stream at 70°C or 700°C can have the same energy, but for the latter it will have a higher exergy. This method preferential selected as it allows a rigorous thermodynamic comprehension of the process. Indeed, a classical energy analysis according to the first law of thermodynamics cannot quantify and spot irreversibilities in a process. Exergy analysis is based on the second law of thermodynamics and allows therefore the identification of losses in the process [29]. Another advantage with exergy analysis is that it does not consider the nature of the thermal input at the heater H-2, but only its temperature.

5.2.1 Assumptions and methodology

As said in the previous section, the PHE of the bottoming cycle is located on the anode exhaust stream. Moreover, the heat exchanger HX-a2 preheats the sweep air with the anode outlet. Therefore, the control volume considered in the following analysis only considers the air and oxygen streams since the integration of the bottoming cycle will solely impact streams within this control volume. Besides in the SOE, water and hydrogen streams do not interact with air/oxygen streams, and consequently they are not considered in the analysis. The control volume is shown in Fig. 5.4.

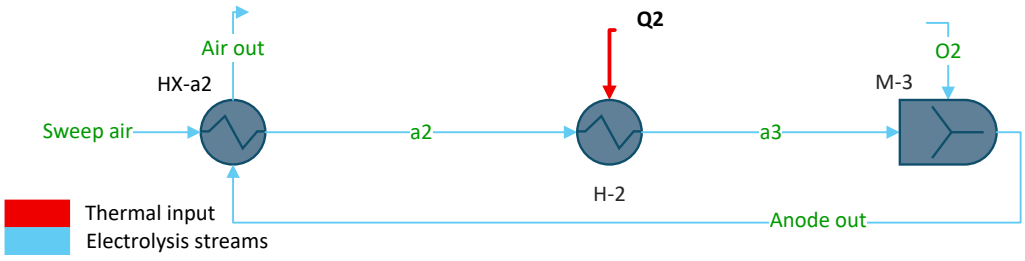

Figure 5.4: *Base case control volume for exergy analysis.*

Exergy must be defined in relation to environment conditions. The environment is considered to have the following properties:

- Temperature T_0 of 20 °C.
- Pressure p_0 of 101.325 kPa.

The specific exergy of a stream is defined as [29]

$$e = e_{PH} + e_{KN} + e_{PT} + e_{CH} \tag{5.4}$$

where the acronyms respectively refer to physical, kinetic, potential and chemical exergy. Kinetic and potential exergy variation are negligible in the process. Chemical exergy variation is neglected, as the only component where such a variation occurs is in the mixer M-3 when the sweep air and oxygen are mixed.

However, considering the much lower ratio of oxygen to the sweep air, the variation is negligible. Finally, the specific exergy of a stream sums up to the physical specific exergy and can be expressed as

$$e = (h - h_0) - T_0(s - s_0) \tag{5.5}$$

where h_0 and s_0 are the dead-state specific enthalpy and entropy.

For a thermal power $\dot{Q}$ at temperature T_b, the associated exergy rate consists in applying the Carnot factor:

$$\dot{E}_{th} = \dot{Q} \cdot (1 - \frac{T_0}{T_b}) \tag{5.6}$$

Whereas for an electrical input, the exergy rate equals the electrical power directly, without any correctional factor.
For a closed system at steady-state, the exergy balance is [29]

$$0 = \sum_j (1 - \frac{T_0}{T_j})\dot{Q}_j - \dot{W}_{cv} + \sum_i \dot{m}_i e_i - \sum_o \dot{m}_o e_o - \dot{E}_D \tag{5.7}$$

where the subscripts cv, i and o respectively denote control volume, inlet, and outlet. The last term is the exergy destruction rate $\dot{E}_D$.

Exergy destruction is the term representing the irreversibilities within the control volume. Besides exergy destruction, exergy loss also occurs. It represents the exergy transferred to the surroundings of the system, and therefore that cannot be valorized [29]. In this work, it is assumed that no exergy losses occurs.

The system being completely defined, an exergy balance on each component can be done. The paper from Valverde et al. [39] details an exergy analysis from a process modelled in Aspen HYSYS™. Their work has thus been used as a guide in the current analysis. First, the exergy balance on the heat exchanger HX-a2 leads to:

$$\dot{E}_{D,HX-a2} = (\dot{m}_{anode,out} \cdot e_{anode,out} + \dot{m}_{sweep,air} \cdot e_{sweep,air}) - (\dot{m}_{air,out} \cdot e_{air,out} + \dot{m}_{a2} \cdot e_{a2}) \tag{5.8}$$

For the heater H-2, the thermal input is assumed to be at 700°C. The exergy balance on H-2 results in:

$$\dot{E}_{D,H-2} = (\dot{Q}_2 \cdot (1 - \frac{T_0}{973.15}) + \dot{m}_{a2} \cdot e_{a2}) - (\dot{m}_{a3} \cdot e_{a3}) \tag{5.9}$$

The balance at the mixer M-3 gives

$$\dot{E}_{D,M-3} = (\dot{m}_{a3} \cdot e_{a3} + \dot{m}_{O2} \cdot e_{O2}) - (\dot{m}_{anode,out} \cdot e_{anode,out}) \tag{5.10}$$

Finally, the exergy loss ratio [29], can be defined as

$$y_D = \frac{\dot{E}_D}{\dot{E}_{D,tot}} \tag{5.11}$$

and represents the ratio of exergy destruction in a component to the total exergy destruction within the system.

5.2.2 Base case

The results are displayed in Table 5.4 . Nearly all exergy destruction occurs in the heat exchanger HX-a2 while exergy rate destructions in the heater H-2 and mixer M-3 are negligible.

In a heat exchanger, exergy destruction occurs because of the heat transfer across a finite temperature difference [29]. Although the exergy rate destruction in each heat exchanger has been computed by an exergy balance, the exergy rate destruction can also be expressed according to [29] as:

$$\dot{E}_D = T_0 \cdot \dot{Q} \cdot \frac{T_{ha} - T_{ca}}{T_{ha} T_{ca}} \tag{5.12}$$

Where T_{ha} and T_{ca} are respectively the average temperatures for the hot and cold streams. This result shows that the temperature difference between the streams is a driving force of the exergy destruction. For H-2, the streams entering the components are close regarding their temperature, as *a*2 is at 680°C and the thermal input is assumed to be at 700°C. For M-3, the two streams have the same temperatures when mixed. For these reasons, the exergy destruction rates in H-2 and M-3 are low compared to the one occurring in HX-a2 where the difference of the average temperatures is more significant.

Table 5.4: *Exergy balance data for the base case control volume.*

Stream	Exergy rate (W)	Component	$\dot{E}_D$ (W)	y_D (%)
Sweep air	−5.10	HX-a2	138.85	99.8
O2	93.31	H-2	0.34	0.2
a2	1631.13	M-3	$< 10^{-3}$	≈ 0
a3	1706.80			
anode out	1800.11			
Q2	76.01			
air out	25.03	**Total**	**139.19**	

Finally, a visual representation of the exergy flows can be done using a Grassmann diagram in Fig. 5.5. This type of diagram consists of applying the same concept of a Sankey diagram with the exception of the arrows being exergy flows. A Grassmann diagram is the most consistent schematic in the current process. Indeed, a Sankey diagram does not differentiate a thermal stream from an electrical one, as it is built on the first law of thermodynamics which implies treating electrical and thermal streams as equivalent quantities.

In Fig. 5.5, it can be observed that the exergy recuperation in HX-a2 is efficient, as the exergy input from Q2 is relatively low compared to the exergy that the stream *Anode out* exchanges with the *Sweep air* stream. Also, *Air out* has a much lower exergy compared to *a2*. The exergy rate destruction is mainly attributed to HX-a2. The exergy destruction from M-3 is not represented considering its negligible value. The total exergy destruction rate is denoted by "E_D TOTAL".

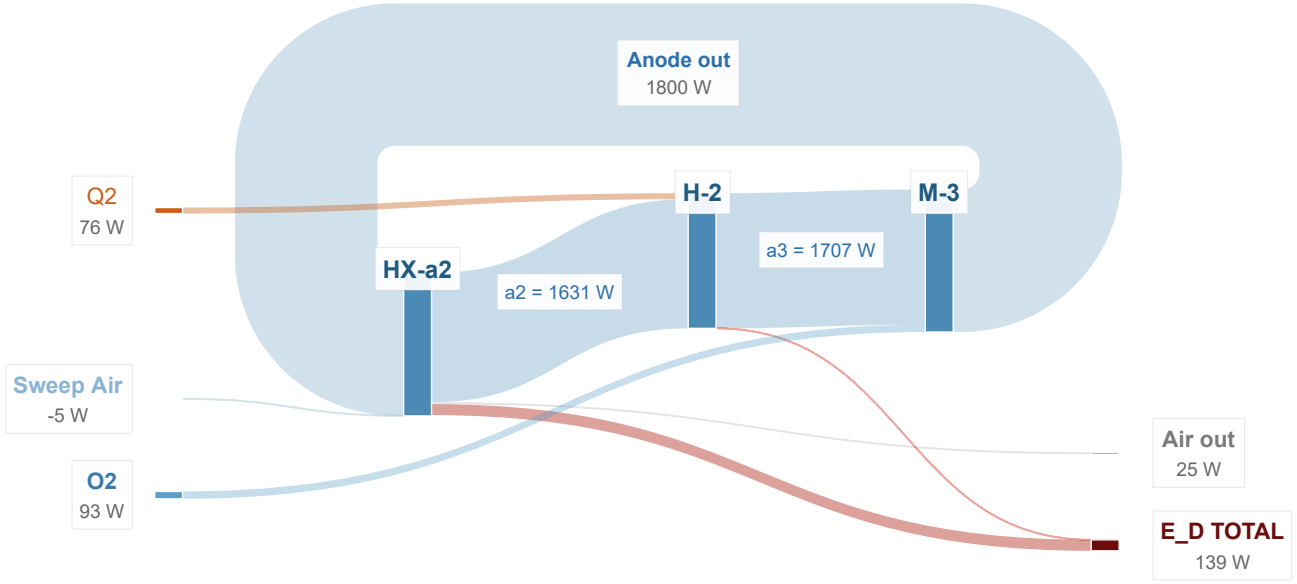

Figure 5.5: *Base case Grassmann diagram.*

5.2.3 Cycle case

Integrating the bottoming cycle leads to the updated control volume in Fig. 5.6. The cycle represented in the schematic is the simple recuperative cycle but the integration with the recompressed recuperative configuration will also be assessed.

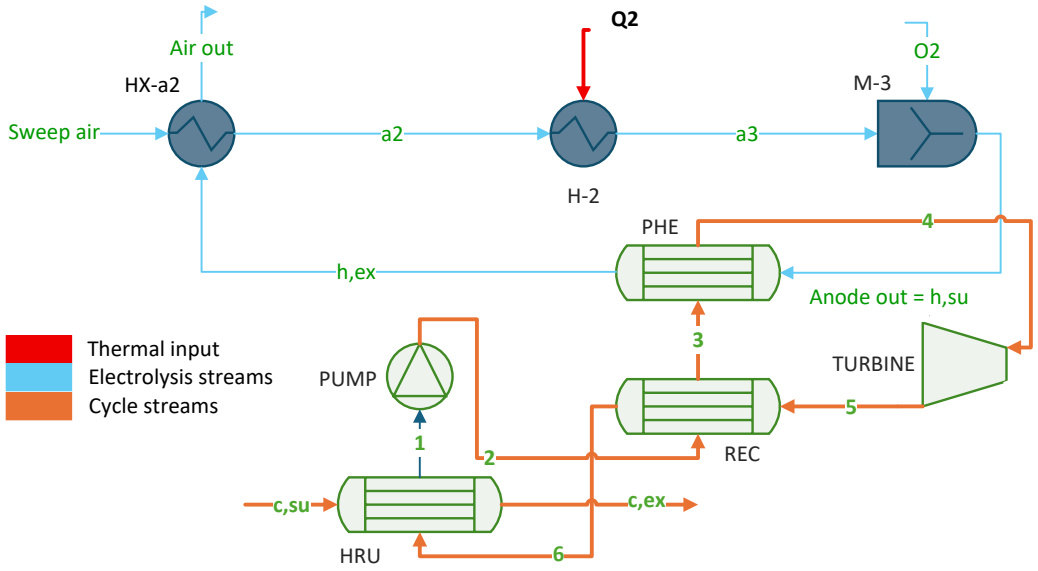

Figure 5.6: *Exergy analysis control volume with bottoming cycle.*

The cycle has two exergy inputs (the hot and cold source inlet streams) and three exergy outputs (the hot and cold source outlet streams), as well as the net power produced. Altogether, this results in the following exergy balance on the cycle:

$$\dot{E}_{D,cycle} = (\dot{m}_{h,su} \cdot e_{h,su} + \dot{m}_{c,su} \cdot e_{c,su}) - (\dot{m}_{h,ex} \cdot e_{h,ex} + \dot{m}_{c,ex} \cdot e_{c,ex} + \dot{W}_{cycle}) \tag{5.13}$$

The total exergy destruction expression is updated:

$$\dot{E}_{D,tot} = \dot{E}_{D,HX-a2} + \dot{E}_{D,H-2} + \dot{E}_{D,M-3} + \dot{E}_{D,cycle} \tag{5.14}$$

To assess the impact of the cycle integration on the total exergy destruction, the two cycle configurations (simple recuperative and recompressed recuperative) can be compared by analysing how the total exergy destruction evolves as a function of the cooling grade.

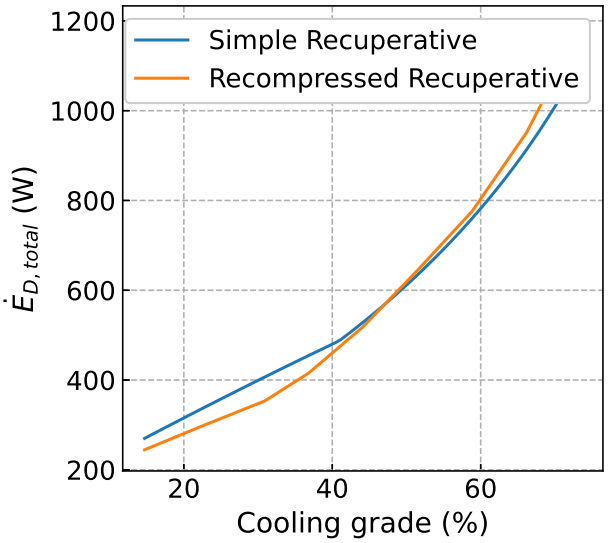

Figure 5.7: *Total exergy destruction rate as a function of the hot source cooling grade for simple and recompressed recuperative configurations.*

The trend in Fig. 5.7 is the same for both configurations: the total exergy destruction is an increasing function with the hot source cooling grade. On a first cooling grade range, the recompressed recuperative cycle is more efficient than the simple recuperative one from an exergy point of view. Then, the behaviour is the opposite from around 45% cooling grade. This phenomenon was the same with the first law efficiency as explained in Section 5.1.2.

To understand the reason of the increasing exergy destruction associated with the cycle implementation, the analysis will be restricted to one cycle configuration: the simple recuperative one. Considering the global trend in Fig. 5.7 to be the same for both configurations, it is expected that results from a comparison between the base case and the case with a simple recuperative cycle would lead to the same conclusions as with a recompressed recuperative cycle.

Considering a 45% cooling grade of the hot source, the exergy balance results are shown in Table 5.5.

Table 5.5: *Exergy balance data with the simple recuperative bottoming cycle for 45% hot source cooling grade.*

Stream	Exergy rate (W)	Component	$\dot{E}_D$ (W)	y_D (%)
Sweep air	−5.10	HX-a2	78.15	14.52
O2	93.31	H-2	111.73	20.76
a2	611.86	M-3	$< 10^{-3}$	≈ 0
a3	1706.80	Cycle	348.19	64.71
ano out	1800.11			
Q2	1206.67			
air out	10.31			
h ex	705.42	**Total**	**538.07**	

Compared to the base case, the exergy destruction rate is much higher, meaning this configuration leads to more irreversibilities and is thus less thermodynamically advantageous. As less heat is available for preheating the sweep air, the average temperatures on each side of the heat exchanger HX-a2 are closer. For this reason, the exergy destruction rate is lower. However, as the sweep air recovers less heat than the previous case, the temperature difference between the thermal input Q2 and the stream *a2* increases, thus explaining the increase in the exergy destruction at the heater H-2. Conclusively, the cycle represents the most significant part of the exergy destruction. The updated Grassmann diagram is shown in Fig. 5.8. Compared to the previous case, it is clear that the exergy input from Q2 and the total exergy destruction both significantly increase.

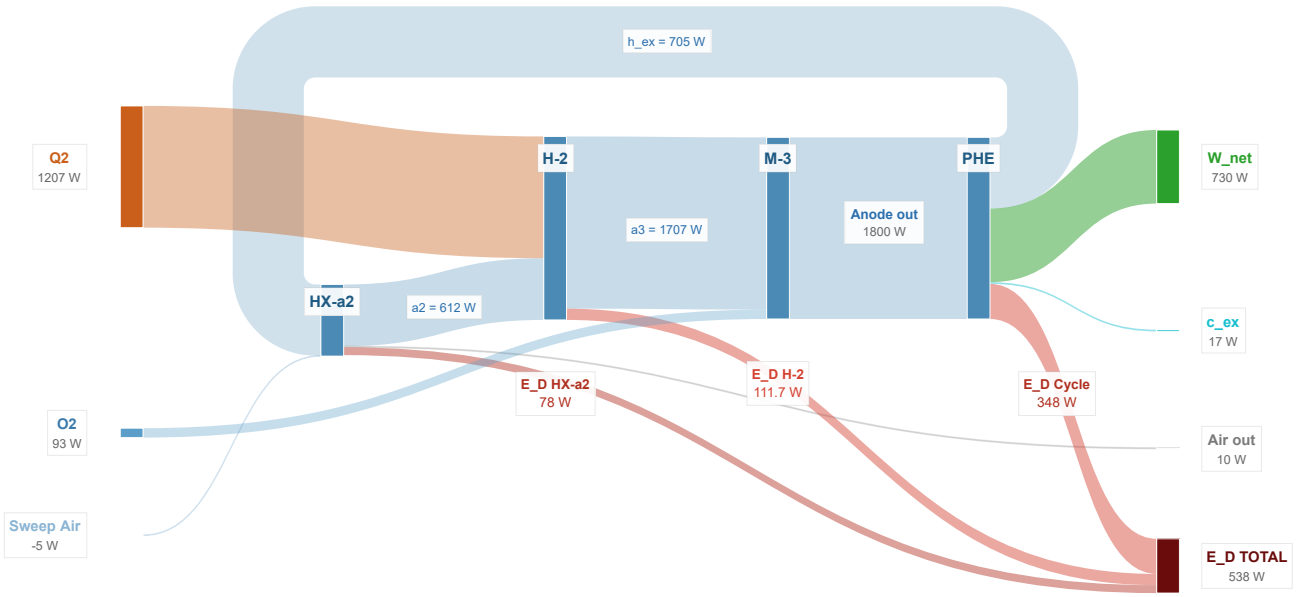

Figure 5.8: *Grassmann diagram with simple recuperative configuration for a 45% hot source cooling grade.*

To better understand why the exergy destruction in the cycle is so important, the exergy rates and exergy destruction rates are computed within the cycle, that is, for each cycle stream and component. The results are displayed in Table 5.6.

Table 5.6: *Exergy balance on the simple recuperative bottoming cycle for 45% hot source cooling grade.*

Stream	Exergy rate (W)	Component	$\dot{E}_D$ (W)	y_D (%)
1	639.3	Compressor	33.95	9.73
2	810.4	Recuperator	159.7	45.80
3	1662	PHE	29.26	8.39
4	2728	Turbine	60.07	17.23
5	1734	HRU	65.75	18.86
6	722.1	**Total**	**348.7**	

The recuperator is where nearly half of the exergy destruction occurs. From Equation 5.12, it is known that exergy destruction is proportional to the heat duty multiplied by the temperature difference in the relevant heat exchanger. Fig. 5.9, demonstrates that both highest duty and average temperatures difference occurs in the recuperator, leading to this high destruction rate. The second element destroying the most exergy is the HRU. Although the heat duty is the least among the heat exchangers, the increase of the heat capacity of the carbon dioxide near the critical point forces the low temperature variation of the

cooling air. As a consequence, the average temperature difference between hot and cold streams becomes significant, leading to a high exergy destruction.

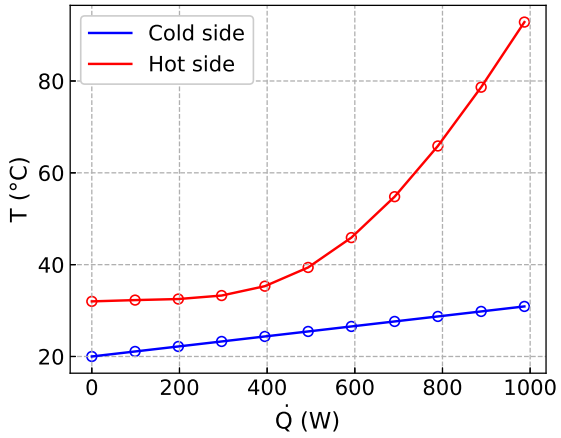

(a) *Heat Rejection Unit.*

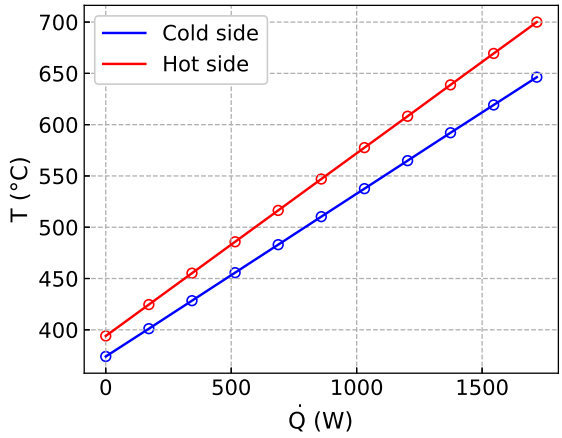

(b) *Primary Heat Exchanger.*

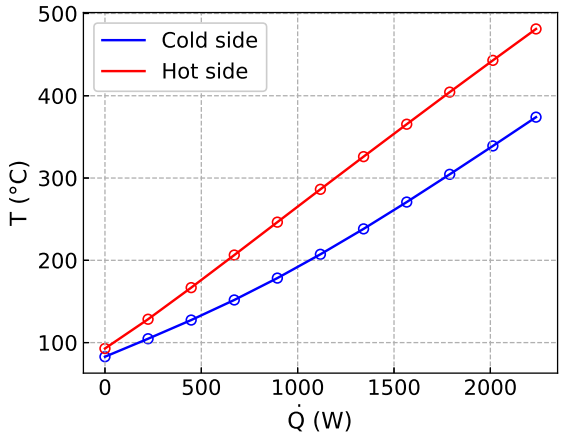

(c) *Recuperator.*

Figure 5.9: *T-Q profiles in heat exchangers of the simple recuperative cycle for a 45% cooling grade.*

5.2.4 Conclusion

From an exergy point of view, the integration of a bottoming cycle does not yet appear to prove a net advantage. Although the integration of a bottoming cycle enables the production of exergy, because of the high exergy destruction occurring within the cycle, the additional exergy destruction is not counterbalanced by the net exergy (net electrical power) produced by the cycle. This preliminary analysis suggests that the initial heat integration with only two heat exchangers for recuperation remains more advantageous.

5.3 Primary energy analysis

The previous analysis demonstrated that, from an exergy point of view, powering a bottoming cycle increases irreversibilities compared to the base case without any cycle. In practice, the trade-off would require a rigorous economic analysis. As such an analysis is beyond the scope of this work, an alternative methodology is used.

The methodology focuses on minimising the total energy consumption of the process. The struggle comes from the inherent difference between thermal and electrical energy inputs. A solution is to convert both energy types to primary energy. In this section, the electricity is considered to be provided by a fictional external grid while the heat input at heaters H-1 and H-2 is deemed to be from the consumption of natural gas. Indeed, natural gas is the dominant fuel in the industry when it comes to medium to high temperature process heating [40].

The primary energy factor (PEF) for electricity is 2.5 in Europe [41] while 1.1 for the natural gas [42], accounting for the losses between production and effective consumption. These factors are expressed as kWh (primary energy) / kWh (energy input). The primary energy considered by the sources is not one specific kind of energy. Rather, it is the amount of energy from all primary energy sources that is needed to deliver and generate that kWh of the energy input (electricity or heat).

These primary energy factors are then applied to the respective inputs in the process. The function to minimise is the specific primary energy consumption (*spec*) and is defined as

$$spec = \frac{f_{th} \cdot (\dot{Q}_{H-1} + \dot{Q}_{H-2}) + f_{el} \cdot (\dot{P}_{SOEC} - \dot{W}_{cycle})}{\dot{m}_{H_{2,out}}} \quad (\mathrm{kWh}_{PE}/\mathrm{kg}_{H_2}) \tag{5.15}$$

where $\dot{P}_{SOE}$ and $\dot{m}_{H_{2,out}}$ are respectively the electrical power consumption of the SOEC and the net hydrogen production. This function represents the amount of primary energy needed to produce one kilogram of hydrogen.

The variable parameter in the optimisation is the heat input given to the cycle, or equivalently, the hot source outlet (*Anode out*) temperature after passing through the PHE. Indeed, the hot source mass flow rate and inlet temperature are fixed. In Equation 5.15, this variation of the heat given to the cycle, $\dot{Q}_{PHE}$, will affect solely $\dot{Q}_{H-2}$ as the cycle takes thermal energy from the anode output, further reducing the thermal energy for preheating the inlet sweeping air, and increasing the thermal demand at the heater H-2.

Before analysing the impact of the integration for each bottoming cycle type, the impact of the increase of $\dot{Q}_{PHE}$ on the growth of $\dot{Q}_{H-2}$ can be evaluated, with the annotations referring to Fig. 5.6. The expressions of these parameters are such that:

$$\dot{Q}_{H-2} = \dot{m}_{\mathrm{sweep,air}} \cdot (h_{a3} - h_{a2}) \tag{5.16}$$

and

$$\dot{Q}_{PHE} = (\dot{m}_{\mathrm{sweep,air}} + \dot{m}_{\mathrm{O_2}}) \cdot (h_{\mathrm{h,su}} - h_{\mathrm{h,ex}}) \tag{5.17}$$

First, the heat capacity of pure oxygen and air are comparable, and the mass flow rate of pure oxygen is negligible compared to the sweep air mass flow rate. Then both streams go through approximately the same temperature window as T_{a3} = $T_{\mathrm{ano,out}}$= 700°C, and the difference between T_{a2} and $T_{\mathrm{h,ex}}$ is equal to the pinch of 20 °C imposed at HX-a2. Following these approximations, the ratio of Equations 5.17 and 5.16 simplifies to:

$$\frac{\dot{Q}_{H-2}}{\dot{Q}_{PHE}} \approx \frac{\dot{m}_{\mathrm{sweep\ air}}}{\dot{m}_{\mathrm{sweep\ air}} + \dot{m}_{\mathrm{O_2}}} = 0.95 \tag{5.18}$$

To validate this result, the heat given to the cycle is varied by ranging $T_{\mathrm{h,ex}}$ between 650 and 250°C. The results appears in Fig. 5.10 demonstrating a linear relation, with a slope of 0.9445, confirming the value of 0.95 obtained by the above demonstration.

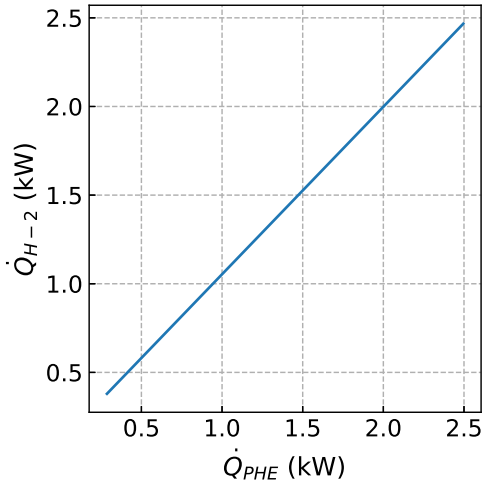

Figure 5.10: *Relation between $\dot{Q}_{H-2}$ and $\dot{Q}_{PHE}$.*

5.3.1 Integration with simple recuperative

Now that the impact of the variation of the heat input at the PHE on the heater H-2 is determined, a first complete integration can be carried out with the simple recuperative configuration. In Fig 5.11, the specific primary energy consumption decreases up to approximately 40% cooling grade. In other words, the total process energy consumption decreases, implying a less carbon emissive process.

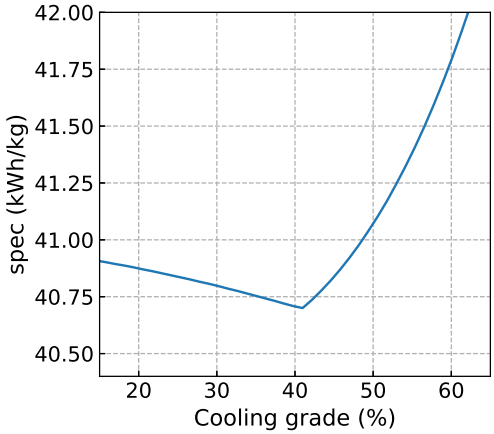

Figure 5.11: *Specific primary energy consumption as a function of the hot source cooling grade for the simple recuperative configuration.*

The decrease of the *spec* occurs when the derivative of the *spec* with respect to the cooling rate is negative. This is equivalent to taking the derivative with respect to $T_{h,ex}$, the PHE's outlet hot source temperature.

$$\frac{d(spec)}{dT_{h,ex}} = f_{th} \cdot \frac{d(\dot{Q}_{H-2})}{dT_{h,ex}} - f_{el} \cdot \frac{d(\dot{W}_{cycle})}{dT_{h,ex}} < 0 \tag{5.19}$$

Isolating each term then leads to

$$f_{th} \cdot \frac{d(\dot{Q}_{H-2})}{dT_{h,ex}} < f_{el} \cdot \frac{d(\dot{W}_{cycle})}{dT_{h,ex}} \tag{5.20}$$

Isolating the primary energy factors and considering Equation 5.18, the relation simplifies to:

$$0.95 \cdot \frac{f_{th}}{f_{el}} < \frac{d(\dot{W}_{cycle})}{d(\dot{Q}_{PHE})} \tag{5.21}$$

The cycle efficiency is a function of $\dot{Q}_{PHE}$. Indeed, it was seen in Section 5.1.2 that from around 40% cooling grade, the cycle efficiency would start to drop. The net cycle power can therefore be expressed as:

$$\dot{W}_{cycle} = \eta_{cycle}(\dot{Q}_{PHE}) \cdot \dot{Q}_{PHE} \tag{5.22}$$

Equation 5.21 becomes:

$$0.95 \cdot \frac{f_{th}}{f_{el}} < \eta_{cycle}(\dot{Q}_{PHE}) + \dot{Q}_{PHE} \cdot \left.\frac{d\eta_{cycle}}{d\dot{Q}_{PHE}}\right|_{\dot{Q}_{PHE}} \tag{5.23}$$

From 0 to approximately 40% cooling grade, the cycle efficiency stays constant. The inequality from Equation 5.23 simplifies to:

$$0.95 \cdot \frac{f_{th}}{f_{el}} = 0.418 < \eta_{cycle} \tag{5.24}$$

The ratio f_{th}/f_{el} equals to 0.44. The maximum efficiency of the simple recuperative cycle is constant and equal to 43.8% for cooling grades below approximately 40% . Equation 5.24 shows that the *spec* decreases, its derivative is negative, as the cycle is efficient enough for an increase of net power to reduce the total system primary energy consumption.

As explained in Section 5.1.2, the cycle efficiency, when reaching around 40% cooling grade, will decrease. Due to this phenomenon, in Fig. 5.11, it is illustrated that from around 40% cooling grade, the decrease in cycle efficiency leads to an increase in the specific primary energy consumption. Indeed, the right second term in Equation 5.23 is negative, as the cycle efficiency decreases with increasing thermal power given to the PHE.

In overall, the minimum *spec* that can be obtained is 40.7 (kWh/kg). Without any bottoming cycle, the *spec* is 40.98 (kWh/kg). Therefore, integrating the simple recuperative configuration results in a relative decrease of the total primary energy consumption of 0.7%. This result shows that integrating a bottoming cycle can indeed exploit the high-temperature exhaust and improve the process efficiency in terms of primary energy consumption.

5.3.2 Integration with recompressed recuperative

Finally, the primary energy optimization is done with the recompressed recuperative sCO_2 cycle as shown in Fig. 5.12

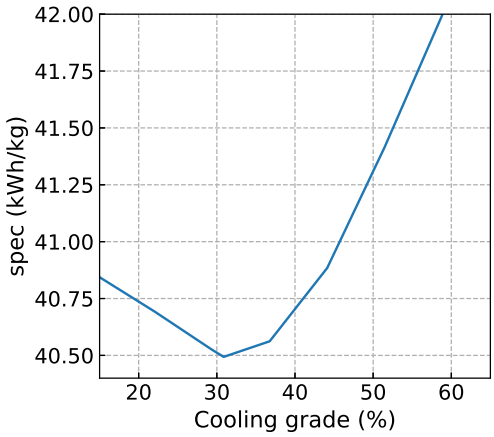

Figure 5.12: *Specific primary energy consumption as a function of the hot source cooling grade for the recompressed recuperative configuration.*

In Fig. 5.12, the curve demonstrates a slightly lower minimum than in the previous case, leading to a decrease of 1.17% of *spec* relative to the case without the cycle. As before, the same behaviour appears, as the efficiency of the bottoming cycle starts to decrease from around 30% cooling degree, such that the specific primary energy consumption increases. Considering the relative low reduction of *spec*, this configuration does not offer any significant advantage compared to the previous case.

5.3.3 Criticism of the methodology

Although this methodology offers an easy comprehension of the problem, it is limited by the accuracy of the primary energy factors. Indeed, the value of the primary energy factor varies over times and depends on the methodology adopted. In Europe, a value of 2.5 has been used as a reference for a long time, while recent regulatory discussions aim to fix this value at 2.1 [41]. However, a study from the FfE [43] reports a higher value of 2.81 using a different methodology. This discrepancy illustrates how results based on primary energy factors have to be interpreted with caution.

The value of 2.5 for the electricity primary energy factor only applies to Europe. However, values of PEF can vary significantly from one country to another. A 2021 report from the IEA [44] stated that primary energy factors for electricity lie in the range 1.25-3.75 worldwide.

Fig. 5.13 displays the relative decrease of the *spec* between the reference case (without bottoming cycle) and with the cycle (simple recuperative configuration) for different electricity primary energy factors. For each f_{el}, the *spec* computed is the one that minimizes this value, as seen in Fig. 5.11.

First, results are displayed for f_{el} above 2.4. Indeed, below this threshold, the addition of the bottoming leads to a higher *spec* compared to the base case, regardless of the cooling grade. The conclusion from this graph is that the higher the carbon intensity of the electricity from the grid, the higher the relevance of using a bottoming cycle.

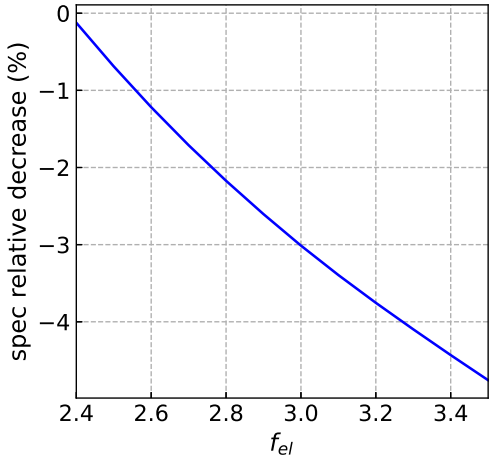

Figure 5.13: *Relative decrease of the specific primary energy consumption at optimal cooling grade as a function of the electricity primary energy factor.*

5.3.4 Transposition to an economic perspective

Although a thorough economic analysis is not included in this study, the operation cost of the process can be approximated, as the primary energy factors in Equation 5.15 can be replaced by price factor, respectively 0.0605€ per kWh for natural gas [45] , and 0.1837€ per kWh for electricity [46]. These values are averages on the European Union level.

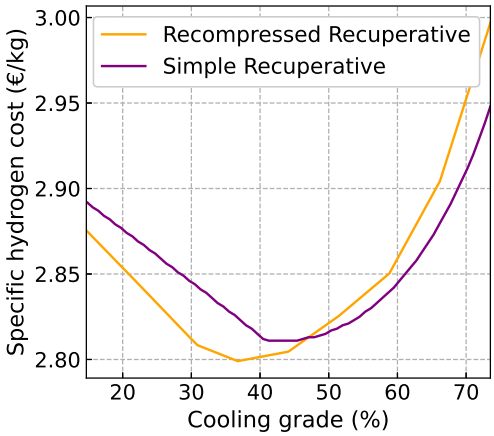

Figure 5.14: *Specific hydrogen operational cost as a function of the cooling grade for the two cycle configurations.*

Although the real economic indicator should be the levelized cost of hydrogen (LCOH), the trend displayed in Fig. 5.14 shows that the minimum cost obtained is around 2.80 € per kg of hydrogen while in the reference case, the cost is 2.93 € per kg of hydrogen. This shows that, even before considering all the costs related to the cycle, integration a bottoming cycle can decrease the cost related to the energy demand of the process. However, the relative difference is such that the additional cycle equipment costs could cause the total cost to surpass that of the reference case.

5.4 Maximisation of the cycle net power

Although the two previous analyses did not demonstrate a significant advantage from the use of a bottoming cycle, it can be interesting to assess a scenario in which one maximises the net power delivered by the bottoming cycle.
The last approach is to consider different cases in which there is no trade-off between thermal and electrical inputs but instead cases where a minimisation of the total electrical consumption is prioritised. Such cases are:

- Off-grid plant operation;
- Low thermal input prices. For instance, heat from concentrated solar power (CSP) could enter into such a category. Let it be known that CSP was not investigated in the primary energy analysis, as it is not possible to assign a primary energy factor to this source. Biomass combustion is also a solution and has the advantage of not being weather dependent.

Minimisation of the total process electrical consumption means maximising the net power produced by the bottoming cycle. As seen in Section 5.1.2, the simple recuperative cycle proved to be the most efficient for high cooling grades, and is thus considered for the current scenario.

To select the point of operation that maximises the cycle net power, the cooling grade is varied as illustrated in Fig. 5.15.

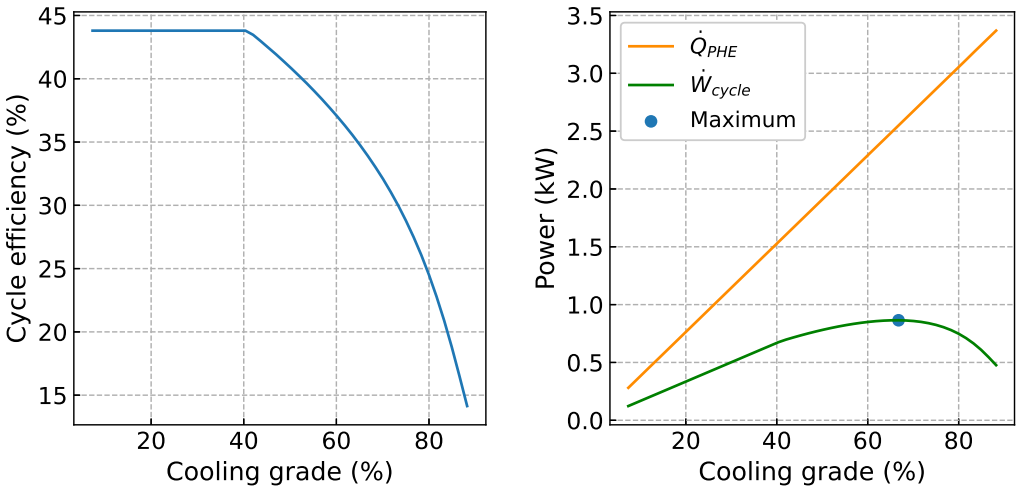

(a) *Cycle efficiency.* **(b)** *Net power and thermal power at the PHE.*

Figure 5.15: *Simple recuperative cycle characteristics as a function of the cooling grade.*

In Fig. 5.15b, the net power of the cycle reaches a maximum with a 66% cooling grade, after which the value decreases. At the maximum, the cycle produces a net power of 865 W. Considering the 4.3 kW SOEC electrical demand, the cycle is able to cover approximately 20% of this demand.

This decrease of the cycle power after 66% cooling grade can be explained through the link between the cycle efficiency, the net power, and the thermal power at the PHE.

$$\dot{W}_{cycle} = \eta_{cycle} \cdot \dot{Q}_{PHE} \tag{5.25}$$

As the thermal power at the PHE increases monotonously with cooling grade but the cycle efficiency drops from 66% cooling grade, the net power cannot increase any further. The selected point of operation for

this section is thus the one at maximum net power. The cycle characteristics at this point are shown in Table 5.7.

Table 5.7: *Simple recuperative cycle state characteristics for a 66% hot source cooling grade.*

State	T (°C)	P (bar)	h (kJ/kg)	s (kJ/kg·K)
1. Compressor inlet	32	76	-191.7	-1363
2. Compressor outlet	82.83	300	-150.3	-1340
3. PHE inlet	230	300	107.7	-725.8
4. Turbine inlet	460.8	300	409.3	-230.7
5. Turbine outlet	315.7	76	264.7	-190
6. HRU inlet	92.83	76	6650	-743.5

At this high cooling grade, the cycle efficiency is low, meaning a high share of the heat given to the cycle is rejected at the HRU. It is therefore relevant to assess the characteristics of this thermal output.

5.4.1 Cooling air

In the current configuration, the cooling air mass flow rate is approximately 30 times higher than the hot source mass flow rate. Considering the scale of the targeted 1 MW plant, the waste energy from this stream cannot be neglected.

An initial problem arises from the relatively low temperature of the outlet cooling air of 30.9°C. This low value is a consequence of the combination of two effects. As the pinch value is imposed and since the carbon dioxide heat capacity increases drastically near the critical point, the flat temperature profile of the carbon dioxide in the HRU near the critical point forces the temperature variation of the cooling air to be low. So, at 30.9°C, the reuse applications of this waste stream are limited.

A solution consists of increasing the compressor supply temperature to allow a higher variation of the cooling air temperature. The results are shown in Figure 5.16.

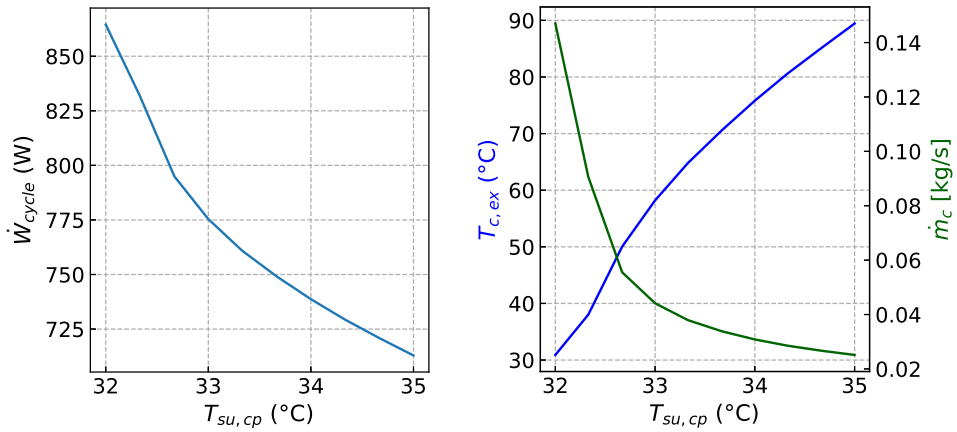

(a) *Net cycle power.*

(b) *Outlet cooling air temperature and cooling air mass flow rate.*

Figure 5.16: *Cycle net power and cooling air characteristics as a function of the compressor supply temperature.*

Fig. 5.16a demonstrates that the cycle net power decreases significantly when the supply compressor tem-

perature increases. By moving slightly away from the critical point, the density rapidly increases, which in turn impacts the compressor power consumption. In Fig. 5.16b, the increase of the compressor supply temperature results in an important decrease of the cooling air mass flow rate but a considerable increase of the cooling air outlet temperature.

Since ambient air is taken as the cooling fluid, there is value in investigating the impact of the ambient temperature on the cooling air leaving the HRU. It should be said that sweep air is ambient air as well, but it has no impact on the cycle performance, as the hot source temperature is 700°C no matter the sweep air temperature. The only impact of a decrease of ambient air temperature is an increase of the thermal demand at the heater H-2, as the sweep air is colder.

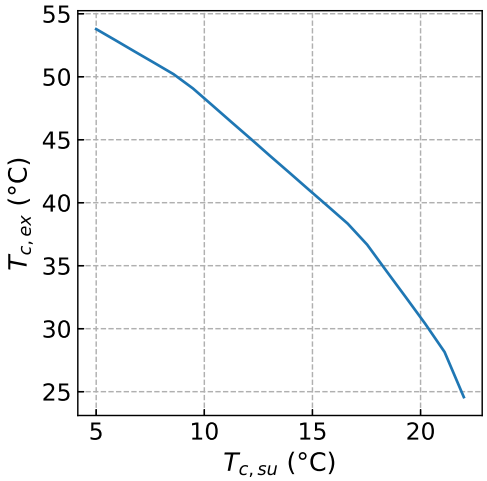

Figure 5.17: *Outlet cooling air temperature as a function of the ambient air temperature.*

As displayed in Fig. 5.17, when the ambient air temperature diminishes, there is an augmentation of the outlet cooling air temperature. At first glance, it appears counter-intuitive. To understand this behaviour, the HRU T-Q profiles are displayed for two different cases below.

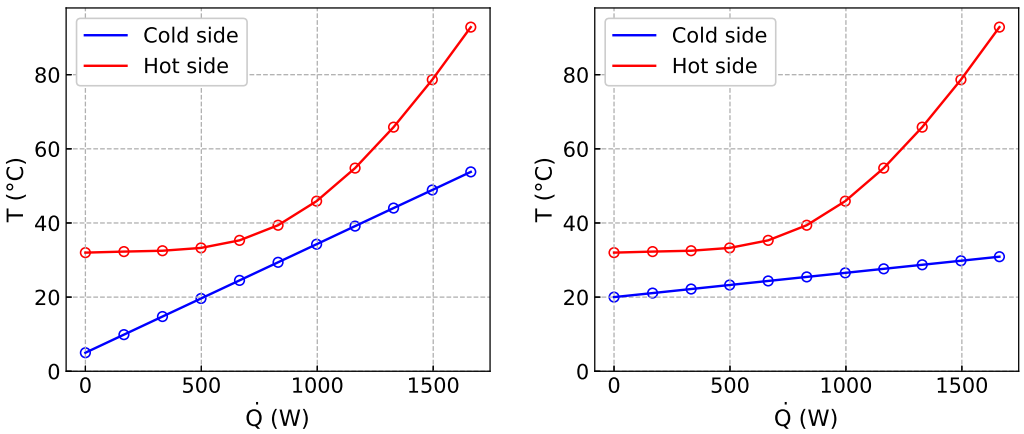

(a) *Ambient temperature of 5 °C.* **(b)** *Ambient temperature of 20 °C.*

Figure 5.18: *T-Q profiles in the heat rejection unit for respectively, an ambient temperature of 5 °C (a) and 20 °C (b) .*

In the simulation, the pinch is imposed. By observing Fig. 5.18, one sees that the pinch remains an

internal pinch in both cases. Due to this constraint, the outlet temperature is higher in the case of the ambient temperature of 5°C. Also, in the latter case, the mass flow rate decreases; the thermal power that has to be rejected remains the same but the cooling air temperature variation increases.

The inlet cooling air temperature was varied between 5 and 22 °C. Considering that the supply temperature at the compressor is fixed at 32° and that the PPTD is set at 10°C, the upper bound of $T_{c,su}$ is 22 °C. Therefore, for places where ambient air temperature exceeds 22 °C, two solutions exist. Provided the compressor inlet temperature remains unchanged, the heat exchanger size can be increased to allow a lower pinch. The other solution is to use water as the cooling medium.

5.4.2 Thermal demand met by hydrogen

For the scope of maximising auto-consumption, the thermal heat provided in heaters H-1 and H-2 can be considered to be provided by the combustion of a fraction of the hydrogen produced by the process.

Up to now, the heat addition in heaters H-1 and H-2 was modelled by respectively $\dot{Q}_1$ and $\dot{Q}_2$. Let's theoretically model the heat addition by hydrogen burners for which η_b represents the burner efficiency, assumed to be equal to 0.9. The fraction f of produced hydrogen needed for the heating requirements can be computed such that:

$$\dot{Q}_1 + \dot{Q}_2 = f \cdot LHV_{H_2} \cdot \eta_b \cdot \dot{m}_{H_2,out} \tag{5.26}$$

Where LHV_{H_2} is the lower heating value of hydrogen, which is equal to 120 MJ/kg [47] and $\dot{m}_{H_2,out}$ the net mass flow rate of hydrogen produced. Table 5.8 summarises parameters for Equation 5.4.2.

Table 5.8: *Parameter values when the thermal demand of the process is met by a fraction of the produced hydrogen.*

Parameter	$\dot{Q}_1$ (W)	$\dot{Q}_2$ (W)	η_b	LHV_{H_2} (MJ/kg)	$\dot{m}_{H_2,out}$ (kg/h)
Value	990	2467	0.9	120	0.2918

Solving Equation 5.4.2 leads to a fraction f of 39.49%. It should be said that this scenario of burning a fraction of the produced oxygen conflicts with the goal of the project, which consists of storing hydrogen. Another possible use of the produced hydrogen would be to use a fraction not to provide the thermal requirements of the process, but to power a cycle. Instead of integrating a bottoming cycle within the process, one could keep the base case without any cycle and burn a fraction of the produced hydrogen to power a cycle and produce electricity. However, as the stored hydrogen is expected to be used after in the discharge mode to produce electricity, the production of electricity through the combustion of hydrogen should be compared with the r-SOC in discharge mode.

5.4.3 Conclusion

The validity of the current scenario can be discussed for the two aforementioned assumptions. The cycle can cover 20% of the stack electrical demand. In case of an off-grid system, the cycle is therefore not able to provide the whole electricity requirements. A combination of a renewable electricity source and a battery system could cover the deficit. Alternatively, instead of using the bottoming cycle within the process, one could dimension the renewable electricity production system such that it would completely meet the stack electrical power needs and recuperate the exhaust high temperature heat from the stack to preheat inlet streams, as done in the base case. Regarding the case for which the heat input is seen as

coming from renewables such as CSP or biomass, the current configuration uses this heat in the heaters within the process while the cycle generates electricity. An alternative approach would be to use the cheap heat to directly power the cycle. In that case, no bottoming cycle is integrated within the process and the high temperature cheap heat powers the cycle, providing the electricity. This reasoning is consistent with that presented in the previous section.

5.5 Summary of the different analyses

Table 5.9 summarises the relevant key numbers and insights from the two main analyses of this work: the primary energy and exergy ones. The analysis for which the net power produced by the cycle is maximised is not included, as it corresponds to a scenario and not an optimisation.

Table 5.9: *Summary of the primary energy and exergy analyses.*

	Primary energy analysis	Exergy analysis
Results	Both cycle configurations, simple recuperative and recompressed recuperative, allow a decrease of the process primary energy consumption, respectively of 0.7% and 1.17%. These benefits stem from the cycles thermal efficiency being greater than the ratio of the primary energy factors.	The minimum exergy consumption of the process is obtained without any bottoming cycle. With both cycle configurations, the exergy destruction increases regardless of the heat given to the cycle. This is attributed to a significant portion of the exergy destruction occurring in the cycle heat exchangers.
Comment	The analysis demonstrates that the integration of both sCO_2 cycle configurations allows the decrease of the carbon emission by the process.	The analysis shows that the exergy destruction occurring within the cycle is too large to counterbalance the net exergy produced by the cycle.
Weakness	The analysis is strongly dependent on the values attributed to primary energy factors. These vary both with the methodology to compute them but also the year.	Do not consider the nature of energy inputs and outputs. Not applicable for a real-case decision but solely to spot the irreversibilities within the system.

Conclusion

This work investigated the integration of a supercritical carbon dioxide Brayton cycle as a bottoming power cycle for the recuperation of high temperature heat from a SOEC. Two different cycle configurations were modelled; simple recuperative and recompressed recuperative layouts. The solid oxide electrolyser stack's anode exhaust was revealed to be the most appropriate location for the bottoming cycle. The reasons are twofold: (1); its approximately 10 times higher heat capacity flow rate compared to the cathode outlet, and (2); the simplicity of a thermal exchange with a hot air stream compared to one with a hydrogen stream. Subsequently, different approaches were used to assess the benefits from this integration, an exergy analysis and a primary energy analysis. Finally, a case where the maximisation of the electricity produced by the cycle was explored.

The exergy analysis demonstrated that adding a bottoming cycle to the process would increase the exergy destruction compared to the reference case without any cycle. Indeed, in the base case, the high exergy recuperation at the air heat exchanger on the sweep air preheating line allowed the exergy input at the sweep air heater to be minimised. Integrating the cycle leads to high irreversibilities, which accounts for 65% of the total exergy destruction. The additional exergy provided by the cycle (the electrical power) is then not significant enough to counterbalance the higher exergy demand at the air heater.

From a primary energy perspective, or equivalently, a carbon emission one, both bottoming cycle configurations showed a decrease in the specific primary energy consumption of the whole process. For the base case, without any bottoming cycle, the specific primary energy consumption of the system is of 40.98 kWh per kg of hydrogen produced. Integrating a bottoming cycle led to a minimum specific primary energy consumption of 40.5 kWh per kg of hydrogen produced. These results prove that powering a bottoming cycle within the process is beneficial compared to a configuration without one. Translating the primary energy analysis into an economic one, it was revealed that, when considering only operational costs (electricity and thermal inputs), integrating the cycle can decrease this operational cost per kg of hydrogen produced by 4.4%. However, this result is less conclusive, as considering the capital expenditures would most likely offset these savings.

Finally, a final approach consisted of maximising the net power output of the cycle in order to minimise the process's electricity consumption. The cycle can provide up to 20% of the process's electrical needs. In this configuration, two additional actions can also be considered. The cooling air can be valorised, at the expense of a lower cycle efficiency. Then, a fraction of the hydrogen burned can be used to meet the thermal needs of the process. This case should, however, be compared with the r-SOC in discharge mode. This scenario of maximising cycle power is coherent in two cases: when the thermal input is provided by cheap heat, such as CSP or biomass, or when the process operates off-grid.

In conclusion, the integration of a bottoming power cycle does not show any evident and clear benefits in terms of carbon emission. The only applications where it would be of use are those in which cheap heat is available. Moreover, the considered thermal input at the heaters in this work is natural gas. However, in real implementations, electrical heaters are used, as they permit a greater level of control. If these were to be considered, a bottoming cycle could be even more disadvantageous.

Appendix

Table 5.10: *Material stream properties in Aspen HYSYS™.*

Stream	Vap. frac.	T (°C)	P (kPa)	ṁ (kg/h)
H2O in	0	25	101.325	1.2925
O2	1	700.099	100	1.0007
Cathode out	1	699.959	100	0.3228
h2tot	1	700	100	0.1415
cat noH2	1	700	100	0.1813
H2 rec	1	700	100	0.0156
H2 no-rec	1	700	100	0.1259
H2 int_rec	1	700	100	0.0154
a3	1	700	100	17.174
H2O rec	0	50.874	100	0.0155
l	0	700	100	0
rea_o	1	700	100	1.3234
w3	0.353	99.591	100	1.3080
SOE_in	1	700	100	1.3234
w4	1	700.027	100	1.3080
cat out 0	1	699.956	100	0.3072
Air out	1	83.242	100	18.174
w1	0	25.306	100	1.3080
H2O_toREC	0	50.874	100	0.0154
cat 1	0.988	50.874	100	0.3072
H2 out	1	50.874	100	0.2918
Sweep Air	1	25	100	17.174
Anode out	1	700.005	100	18.174
a2	1	680.005	100	17.174

Bibliography

[1] Eurostat, "Energy in Europe – 2026 edition," Interactive Publication, Mar. 2026. [Online]. Available: https://ec.europa.eu/eurostat/web/interactive-publications/energy-2026

[2] European Commission, "Joint Statement by the Director-General of the International Renewable Energy Agency La Camera and EU Commissioner Simson: 'The time for speeding up renewables is now'," Mar. 2023. [Online]. Available: https://energy.ec.europa.eu/news/joint-statement-director-general-international-renewable-energy-agency-la-camera-and-eu-commissioner-2023-0 en

[3] P. Jowett, "Germany, France, Netherlands curtail 3.9 TWh of renewables in 2025," Feb. 2026. [Online]. Available: https://www.pv-magazine.com/2026/02/03/germany-france-netherlands-curtail-3-9-twh-of-renewables-in-2025/

[4] International Energy Agency (IEA), "VRE shares in generation and technical curtailment for selected countries," May 2023. [Online]. Available: https://www.iea.org/data-and-statistics/charts/vre-shares-in-generation-and-technical-curtailment-for-selected-countries

[5] M. A. Ancona, G. Brunaccini, A. De Pascale, F. Ferrari, M. Ferraro, C. Italiano, T. Santangelo, and A. Vita, "Performance Analysis of a Power-to-Gas Storage System based on r-SOC," *Journal of Physics: Conference Series*, vol. 2893, no. 1, p. 012051, Nov. 2024. doi: 10.1088/1742-6596/2893/1/012051 .

[6] M. A. Ancona, M. Bianchi, L. Branchini, F. Catena, A. De Pascale, F. Melino, and A. Peretto, "Numerical prediction of off-design performance for a Power-to-Gas system coupled with renewables," *Energy Conversion and Management*, vol. 210, p. 112702, Apr. 2020. doi: 10.1016/j.enconman.2020.112702 .

[7] G. Min, S. Choi, and J. Hong, "A review of solid oxide steam-electrolysis cell systems: Thermodynamics and thermal integration," *Applied Energy*, vol. 328, p. 120145, Dec. 2022. doi: 10.1016/j.apenergy.2022.120145 .

[8] S. G. Nnabuife, C. K. Darko, P. C. Obiako, B. Kuang, X. Sun, and K. Jenkins, "A Comparative Analysis of Different Hydrogen Production Methods and Their Environmental Impact," *Clean Technologies*, vol. 5, no. 4, pp. 1344–1380, Nov. 2023. doi: 10.3390/cleantechnol5040067 .

[9] L. Wang, M. Chen, R. Küngas, T.-E. Lin, S. Diethelm, F. Maréchal, and J. Van Herle, "Power-to-fuels via solid-oxide electrolyzer: Operating window and techno-economics," *Renewable and Sustainable Energy Reviews*, vol. 110, pp. 174–187, Aug. 2019. doi: 10.1016/j.rser.2019.04.071 .

[10] M. Reisert, A. Aphale, and P. Singh, "Solid Oxide Electrochemical Systems: Material Degradation Processes and Novel Mitigation Approaches," *Materials*, vol. 11, no. 11, p. 2169, Nov. 2018. doi: 10.3390/ma11112169 .

[11] J. Freymann, K. Hauptmeier, A. Kamolz, M. Hauer, and S. Kroop, "Assessment of hydrogen certification standards and requirements," Tech. Rep. D4.2, 2020. [Online]. Available: https://salcos.salzgitter-ag.com/fileadmin/footage/MEDIA/SZAG_microsites/salcos/2022/grinhy-20/downloads/deliverables/D4.2-Assessment-of-hydrogen-certification-standards-and-requirements_1.pdf

[12] J. Mougin, J. Aicart, A. Gajewski, A. Agrawal, H. Bergman, and P. Olivier, "Design, laboratory characterization, factory acceptance tests and installation of a 2.6 MW High temperature steam electrolyser in a refinery," *International Journal of Hydrogen Energy*, vol. 141, pp. 1165–1171, Jun. 2025. doi: 10.1016/j.ijhydene.2025.02.070 .

[13] Clean Hydrogen Partnership, "Multimegawatt high-temperature electrolyser to generate green hydrogen for production of high-quality chemical products." [Online]. Available: https://www.clean-hydrogen.europa.eu/projects-dashboard/projects-repository/multiplhy_en

[14] E. Crespi, F. Panaccione, D. Ragaglia, and M. Testi, "Integration of a solid oxide electrolysis system with solar thermal and electrical energy: A testing campaign for operation and control strategy definition," *IET Renewable Power Generation*, vol. 18, no. S1, pp. 4399–4413, Dec. 2024. doi: 10.1049/rpg2.13141 .

[15] F. Wang, L. Wang, H. Zhang, L. Xia, H. Miao, and J. Yuan, "Design and optimization of hydrogen production by solid oxide electrolyzer with marine engine waste heat recovery and ORC cycle," *Energy Conversion and Management*, vol. 229, p. 113775, Feb. 2021. doi: 10.1016/j.enconman.2020.113775 .

[16] Q. Li, H. Machida, and K. Norinaga, "Design and Optimization of Large-Scale Green Liquid Hydrogen Production Integrated with Heat Recovery and Absorption Precooling," *Industrial & Engineering Chemistry Research*, vol. 63, no. 44, pp. 19 063–19 075, Nov. 2024. doi: 10.1021/acs.iecr.4c02383 .

[17] S. S. Niknezhad, F. Moghaddamali, and E. Pistikopoulos, "Toward More Efficient Large-Scale Green Hydrogen Systems via Waste Heat Recovery and ORC," *Applied Sciences*, vol. 15, no. 10, p. 5224, May 2025. doi: 10.3390/app15105224 .

[18] M. Sahdev, "Pinch Technology: Basics for the Beginners," 2009. [Online]. Available: https://www.cheresources.com/invision/index.php?app=core&module=attach&section=attach&attach_id=9707

[19] M. Astolfi, D. Alfani, S. Lasala, and E. Macchi, "Comparison between ORC and CO2 power systems for the exploitation of low-medium temperature heat sources," *Energy*, vol. 161, pp. 1250–1261, Oct. 2018. doi: 10.1016/j.energy.2018.07.099 .

[20] V. Thielens, F. Demeyer, and W. De Paepe, "Performance comparison of sCO 2 and steam cycles for waste heat recovery based on annual semi-transient modeling under complex industrial constraints," *Case Studies in Thermal Engineering*, vol. 60, p. 104691, Aug. 2024. doi: 10.1016/j.csite.2024.104691 .

[21] P. Pidaparti and E. Liese, "Performance and Economic Evaluation of sCO2 Bottoming Cycles for Natural Gas Combined Cycle Plants with Capture," in *The 8th International Supercritical CO2 Power Cycles Symposium*, Feb. 2024. [Online]. Available: https://sco2symposium.com/proceedings2024/32-paper.pdf

[22] Y. Liu, Y. Wang, and D. Huang, "Supercritical CO2 Brayton cycle: A state-of-the-art review," *Energy*, vol. 189, p. 115900, Dec. 2019. doi: 10.1016/j.energy.2019.115900 .

[23] "Carbon dioxide: Phase change data," in *NIST Chemistry WebBook, NIST Standard Reference Database Number 69*. National Institute of Standards and Technology. [Online]. Available: https://webbook.nist.gov/cgi/cbook.cgi?ID=C124389&Mask=4#Thermo-Phase

[24] M. T. White, G. Bianchi, L. Chai, S. A. Tassou, and A. I. Sayma, "Review of supercritical CO 2 technologies and systems for power generation," *Applied Thermal Engineering*, vol. 185, p. 116447, Feb. 2021. doi: 10.1016/j.applthermaleng.2020.116447 .

[25] P. Wu, C. Gao, Y. Huang, D. Zhang, and J. Shan, "Supercritical CO_2 Brayton Cycle Design for Small Modular Reactor with a Thermodynamic Analysis Solver," *Science and Technology of Nuclear Installations*, vol. 2020, pp. 1–16, Jan. 2020. doi: 10.1155/2020/5945718 .

[26] A. Baronci, G. Messina, S. J. McPhail, and A. Moreno, "Numerical investigation of a MCFC (Molten Carbonate Fuel Cell) system hybridized with a supercritical CO 2 Brayton cycle and compared with a bottoming Organic Rankine Cycle," *Energy*, vol. 93, pp. 1063–1073, Dec. 2015. doi: 10.1016/j.energy.2015.07.082 .

[27] Y. Demirel, "Thermodynamic Analysis," *Arabian Journal for Science and Engineering*, vol. 38, no. 2, pp. 221–249, Feb. 2013. doi: 10.1007/s13369-012-0450-8 .

[28] M. Sadeghi, S. M. Seyed Mahmoudi, and M. A. Rosen, "Thermoeconomic analysis of two solid oxide fuel cell based cogeneration plants integrated with simple or modified supercritical CO2 Brayton cycles: A comparative study," *Energy*, vol. 259, p. 125038, Nov. 2022. doi: 10.1016/j.energy.2022.125038 .

[29] A. Bejan, G. Tsatsaronis, and M. Moran, *Thermal Design and Optimization*. John Wiley & Sons, 1996.

[30] A. D. Akbari and S. M. Mahmoudi, "Thermoeconomic analysis & optimization of the combined supercritical CO 2 (carbon dioxide) recompression Brayton/organic Rankine cycle," *Energy*, vol. 78, pp. 501–512, Dec. 2014. doi: 10.1016/j.energy.2014.10.037 .

[31] F-Chart Software, "CARBONDIOXIDE or R744." [Online]. Available: https://fchart.com/ees/eeshelp/carbondioxide_or_r744.htm

[32] J. E. Cha, J. H. Park, G. Lee, H. Seo, S. Lee, H.-J. Chung, and S. W. Lee, "500 kW supercritical CO2 power generation system for waste heat recovery: System design and compressor performance test results," *Applied Thermal Engineering*, vol. 194, p. 117028, Jul. 2021. doi: 10.1016/j.applthermaleng.2021.117028 .

[33] A. Schroder and M. Turner, "Mapping the Design Space of a Recuperated, Recompression, Precompression Supercritical Carbon Dioxide Power Cycle with Intercooling, Improved Regeneration, and Reheat," in *4th International Supercritical CO2 Power Cycles Symposium*, Sep. 2014. [Online]. Available: https://sco2symposium.com/papers2014/systemModelingControl/67-Schroder.pdf

[34] J. Xing, C. Li, Y. Wang, and F. He, "A comparative study on effectiveness method and pinch analysis method in the thermodynamic investigation of supercritical CO2 power cycle," *Energy*, vol. 341, p. 139350, Dec. 2025. doi: 10.1016/j.energy.2025.139350 .

[35] C. White, "Analysis of Brayton Cycles Utilizing Supercritical Carbon Dioxide," National Energy Technology Laboratory (NETL), Tech. Rep. DOE/NETL-4001/070114, Jul. 2014. [Online]. Available: https://netl.doe.gov/projects/files/AnalysisofBraytonCyclesUtilizingSupercriticalCarbonDioxide_070114.pdf

[36] S. Kim, Y. Cho, M. S. Kim, and M. Kim, "Characteristics and optimization of supercritical CO2 recompression power cycle and the influence of pinch point temperature difference of recuperators," *Energy*, vol. 147, pp. 1216–1226, Mar. 2018. doi: 10.1016/j.energy.2017.12.161 .

[37] American Institute of Chemical Engineers, "Hydrogen Flammability," Tech. Rep. [Online]. Available: https://www.aiche.org/sites/default/files/docs/pages/the_elemental_-_hydrogen_flammability.pdf

[38] M. Chase, *NIST-JANAF Thermochemical Tables*, 4th ed., ser. Journal of Physical and Chemical Reference Data, Monograph No. 9. American Institute of Physics, 1998. [Online]. Available: https://webbook.nist.gov/cgi/cbook.cgi?ID=C7782447&Mask=1&Type=JANAFG&Table=on

[39] J. V. Valverde, V. Ferro, L. Postolache, and A. Giroir-Fendler, "Efficient Exergy Analysis of Chemical Processes through Process Engineering Software," *Journal of Computer Science Research*, vol. 6, no. 3, pp. 23–44, Aug. 2024. doi: 10.30564/jcsr.v6i3.6720 .

[40] Centre for International Energy Policy, "European Union Industrial Energy Use with a Focus on Natural Gas," Tech. Rep., Dec. 2017. [Online]. Available: https://ciep.energy/media/pdf/uploads/CIEP_2017__03_web.pdf

[41] E. Parliament, "Revising the primary energy factor for electricity," Tech. Rep. 2022/3021(DEA), Dec. 2022. [Online]. Available: https://oeil.secure.europarl.europa.eu/oeil/en/procedure-document-summary/pdf?id=1727943

[42] T. Duh Čož, A. Kitanovski, and A. Poredoš, "Primary Energy Factor of a District Cooling System," *Strojniški vestnik - Journal of Mechanical Engineering*, vol. 62, no. 12, pp. 717–729, Dec. 2016. doi: 10.5545/sv-jme.2016.3777 .

[43] K. Britta, C. Pellinger, S. von Roon, T. Hubner, and G. Kaestle, "EU Displacement Mix," Research Center for Energy Economics (FfE), Tech. Rep., May 2018. [Online]. Available: https://cogeneurope.eu/wp-content/uploads/2024/07/EU-Displacement-Mix.pdf

[44] International Energy Agency (IEA), "Global Hydrogen Review: Assumptions annex," Tech. Rep., 2021. [Online]. Available: https://iea.blob.core.windows.net/assets/2ceb17b8-474f-4154-aab5-4d898f735c17/IEAGHRassumptions_final.pdf

[45] Eurostat, "Natural gas price statistics," 2026. [Online]. Available: https://ec.europa.eu/eurostat/statistics-explained/index.php?title=Natural_gas_price_statistics#Natural_gas_prices_for_non-household_consumers

[46] Eurostat, "Electricity price statistics," 2026. [Online]. Available: https://ec.europa.eu/eurostat/statistics-explained/index.php?title=Electricity_price_statistics#Electricity_prices_for_non-household_consumers

[47] The Engineering ToolBox, "Higher Calorific Values of Common Fuels: Reference & Data," 2003. [Online]. Available: https://www.engineeringtoolbox.com/fuels-higher-calorific-values-d_169.html